High-Order Spectral Volume Method for the Navier-Stokes Equations On Unstructured Tetrahedral Grids

By

Z.J. Wang
Spahr Professor and Chair of Aerospace Engineering
University of Kansas
2120 Learned Hall, Lawrence, KS 66045
Tel: (785) 864-2440
zjw@ku.edu

Before August 15, 2012
Professor of Aerospace Engineering
Iowa State University
2271 Howe Hall, Ames, IA 50011
Tel: (515) 294-1614
Fax: (515) 294-3262
E-mail: zjw@iastate.edu

December 6, 2012

Final Report
For the period of May 15, 2005 – August 14, 2009
Prepared for
Office of Science
U.S. Department of Energy
1000 Independence Avenue, SW
Washington, DC 20585

DOE Grant Number: **DE-FG02-05ER25677**
DOE Program Manager: **Dr. Anil Deane**

This material is based upon work supported by the Department of Energy under grant number FG02-05ER25677. Any opinions, findings, and conclusion or recommendation expressed in this publication are those of the author(s) and do not necessarily reflect the views of the Department of Energy.

RESEARCH OBJECTIVES

The overriding objective for this project is to develop an efficient and accurate method for capturing strong discontinuities and fine smooth flow structures of disparate length scales with unstructured grids, and demonstrate its potentials for problems relevant to DOE. More specifically, we plan to achieve the following objectives:

1. Extend the SV method to three dimensions, and develop a fourth-order accurate SV scheme for tetrahedral grids. Optimize the SV partition by minimizing a form of the Lebesgue constant. Verify the order of accuracy using the scalar conservation laws with an analytical solution;

2. Extend the SV method to Navier-Stokes equations for the simulation of viscous flow problems. Two promising approaches to compute the viscous fluxes will be tested and analyzed;

3. Parallelize the 3D viscous SV flow solver using domain decomposition and message passing. Optimize the cache performance of the flow solver by designing data structures minimizing data access times;

4. Demonstrate the SV method with a wide range of flow problems including both discontinuities and complex smooth structures.

The objectives remain the same as those outlines in the original proposal. We anticipate no technical obstacles in meeting these objectives.

1. MAJOR ACCOMPLISHMENTS

All the main objectives in this project have been achieved. More specifically, we accomplished the following:

1. Successfully extended the spectral volume method to three dimensions for simplex elements. In addition, we found that the SV method and the SD method are identical in 1D. In order to boost efficiency, a quadrature-free version was developed, which allows the SV method to be implemented for 3D problems much more efficiently that the traditional approach. However, the SV method was still found to be more expensive than several recent method such as the SD method.

2. Successfully extended the SV method to the Navier-Stokes equations. Following ideas in the discontinuous Galerkin (DG) community, several robust techniques have been developed, and are shown to perform satisfactorily.

3. The SV solve has been implemented for parallel computers using domain-decomposition and MPI, and demonstrated excellent scalability because of the compact nature of the SV method.

4. Solution based mesh adaptation has been implemented to further boost the efficiency of the SV method in handling problems with both discontinuities and complex smooth features.

In this report, we elaborate on the solution-based mesh adaptation.

2. Review of the Quadrature-Free Spectral Volume Method

Consider the multidimensional conservation law

$$\frac{\partial Q}{\partial t}+\frac{\partial f(Q)}{\partial x}+\frac{\partial g(Q)}{\partial y}+\frac{\partial h(Q)}{\partial z}=0, \tag{2.1a}$$

on domain $\Omega \times [0,T]$ and $\boldsymbol{\Omega} \subset \boldsymbol{R}^3$ with the initial condition

$$Q(x,y,z,0)=Q_0(x,y,z), \tag{2.1b}$$

and appropriate boundary conditions on $\partial\Omega$. In (2.1), x,y, and z are the Cartesian coordinates and $(x,y,z)\in \Omega$, $t \in [0,T]$ denotes time, Q is the vector of conserved variables, and f, g and h are the fluxes in the x, y and z directions, respectively. Domain Ω is discretized into I nonoverlapping triangular (2D), or tetrahedral (3D) cells. In the SV method, the simplex grid cells are called

SVs, denoted S_i, which are further partitioned into CVs, denoted $C_{i,j}$, which depend on the degree of the polynomial reconstruction. Examples of partitions supporting linear, quadratic and cubic reconstructions are shown in Figure 1.

Volume-averaged conserved variables on the CVs are then used to reconstruct a high-order polynomial inside the SV. To represent the solution as a polynomial of degree m, we need N pieces of independent information, or degrees of freedom (DOFs). Where N is calculated as follows:

$$N = \frac{(m+1)(m+2)\cdots(m+d)}{d!}, \tag{2.2}$$

where d is the spatial dimension of the problem. The DOFs in the SV method are the volume-averaged conserved variables at the N CVs. Define the CV-averaged conserved variable for $C_{i,j}$ as

$$\overline{Q}_{i,j} = \frac{1}{V_{i,j}} \int_{C_{i,j}} Q dV, \quad j=1,\ldots,N, \quad i=1,\ldots,I, \tag{2.3}$$

where $V_{i,j}$ is the volume of $C_{i,j}$. Given the CV-averaged conserved variables for all CVs in S_i, a polynomial $p_i(x,y,z) \in P^m$ (the space of polynomials of at most degree m) can be reconstructed such that it is a $(m+1)^{\text{th}}$ order accurate approximation to $Q(x,y,z)$ inside S_i.

$$p_i(x,y,z) = Q(x,y,z) + O\left(h^{m+1}\right), \quad (x,y,z) \in S_i, \quad i=1,\ldots,I, \tag{2.4}$$

where h is the maximum edge length of all the CVs. This reconstruction can be solved analytically by satisfying the following conditions:

$$\frac{1}{V_{i,j}} \int_{C_{i,j}} p_i(x,y,z) dV = \overline{Q}_{i,j}, \quad j=1,\ldots..,N.$$

(2.5)

This polynomial $p_i(x,y,z)$ is the $(m+1)^{th}$ order approximation we are looking for as long as the solution $Q(x,y,z)$ is smooth in the region covered by S_i. The reconstruction is expressed more conveniently as

$$p_i(x,y,z) = \sum_{j=1}^{N} L_j(x,y,z) \overline{Q}_{i,j}, \tag{2.6}$$

where $L_j(x,y,z) \in P^m$ are the shape functions which satisfy

$$\frac{1}{V_{i,j}} \int_{C_{i,j}} L_n(x,y,z) dV = \delta_{jn}. \tag{2.7}$$

Integrating (2.1) in $C_{i,j}$, we obtain

$$\frac{d\overline{Q}_{i,j}}{dt} + \frac{1}{V_{i,j}} \sum_{r=1}^{K} \int_{A_r} (F \cdot \hat{n}) dA = 0, \qquad j=1,\ldots,N, \qquad i=1,\ldots,I, \tag{2.8}$$

where $F = (f,g,h)$, A_r represents the r^{th} face of $C_{i,j}$, $\hat{n}$ is the outward unit normal vector of A_r, and K is the number of faces in $C_{i,j}$. More details of this, including representative plots of the shape functions can be found in Wang and Liu [29].

A nodal set, such as those shown in Figure 2, is selected from Hesthaven [16] and used to support a degree $m+1$ polynomial reconstruction for the flux vector. The flux vector F can be computed at any point (x, y, z) by the following

$$F(x, y, z) = \sum_{i=1}^{N_S} M_i (x, y, z) F_i \ , \tag{2.9}$$

where N_s is the number of nodes in the nodal set, calculated from (2.2), F_i is the flux vector evaluated at node i , and $M_i(x,y,z)$ are the shape functions defined by the nodal set which satisfy

$$M_n(x_j, y_j, z_j) = \delta_{jn}.$$

(2.10)

Some representative examples of the shape functions are shown in Harris et al [14]. The average of (2.9) over a particular face is given by

$$\overline{F} = \sum_{i=1}^{N_S} \overline{M}_i F_i \ , \tag{2.11}$$

where $\overline{M}_i$ are the face-averaged node-based shape functions for that face evaluated in the standard element. This can be done either analytically using Mathematica [33] or the like, or numerically using Gauss quadrature formulas.

The face integral in (2.8) is then given as

$$\int_{A_r} (F \cdot \hat{n}) dA = A_r \overline{F}_n \ , \tag{2.12}$$

where $\overline{F}_n$ is the dot product of (2.11) with $\hat{n}$. This expression is exact for internal faces. For faces on SV boundaries, we use

$$\int_{A_r} (F \cdot \hat{n}) dA \cong \frac{A_r}{2} \left[\overline{F}_{n,L} + \overline{F}_{n,R} - \alpha_c \left(\overline{Q}_R - \overline{Q}_L \right) \right], \tag{2.13}$$

where $\overline{F}_{n,L}$ and $\overline{F}_{n,R}$ denote the face-averaged normal component of the flux vector due to the SV to the left and right of the interface, respectively, and α_c is taken as the maximum absolute eigenvalue as in the Rusanov flux [22], or the dissipation matrix as in the Roe flux [21], which is evaluated at the face center. $\overline{Q}_R$ and $\overline{Q}_L$ are the face-averaged conserved variables due to the SV to the right and left of the interface, respectively.

3. **Adaptive hp-refinement**

Local adaptive grid refinement is used to focus computational effort near discontinuities and fine smooth features to reduce the overall computational effort in the entire domain. H-refinement involves modification of cell sizes while p-refinement involves modification of polynomial orders. We wish to utilize either or both on-the-fly as the flow develops. Both h- and p-refinements are carried out using only local operations to maximize the efficiency and accuracy of the procedure.

1. H-refinement

In this study, since we are only dealing with triangular SVs, the h-refinement can be performed without introducing the so-called hanging nodes. Therefore, it is basically a matter of grid regeneration, with no required modification of the solver itself. An efficient hierarchical edge-based adaptation algorithm is employed, which allows the grid to be adapted any number of levels from the base (coarsest) grid at any time. Let ε_i be an adaptation indicator for edge i, and let ε_{max} be some norm of ε_i accounting for all edges in the domain. If for any edge i, $\varepsilon_i > \alpha\varepsilon_{max}$, then edge i is split into two edges, otherwise edge i is maintained. Here $\alpha > 0$ is a user specified constant. The value $\alpha = 1$ provides sufficient adaptation in most cases, and is used in all cases considered here, unless otherwise noted. The adaptation procedure begins with edges in the base grid (root edges), and continues until the maximum number of adaptation levels is reached. The adaptation indicator ε_i is always computed using the solution from the previously adapted (finest) grid. When the above procedure completes, new SVs are added to the grid as a result of the split edges. There are essentially four different situations that can occur when the grid is adapted, as shown in Figure 3.

For each SV in the grid, the difference in adaptation level for that SV's edges is allowed to be no greater than one. This is done to prevent the creation of overly skewed cells, so that all grids are comparable in quality to the base grid. When the creation of new SVs is complete, new cell-averages are then computed using

$$\overline{Q}_{i,j} = \sum_{k=1}^{N_S} \overline{M}_{j,k} Q_{i,k} \ , \tag{3.1}$$

where $\overline{M}_{j,k}$ are the node-based shape functions for node k averaged over CV j, and $Q_{i,k}$ are the conserved variables evaluated at node k of SV i. If node k exists within a SV in the previously adapted grid, then $Q_{i,k}$ are obtained from (2.6) using CV-averaged solutions $\overline{Q}_{i,j}$ from that SV. Otherwise, if node k exists at the junction between two or more SVs in the previously adapted grid, then $Q_{i,k}$ are obtained from an average of (2.6) among all SVs which have the physical location of node k in common. The above interpolation gives rise to an inherent loss of precision associated with coarsening of the solution, which is an unavoidable consequence of the h-refinement procedure. Two different methods for computing the adaptation indicator ε_i are given below. The first, and simplest adaptation indicator is computed using

$$\varepsilon_i = \left|\Delta \psi_i\right| A_i^u , \tag{3.2}$$

where $\Delta\psi_i$ is the difference of ψ between the two endpoints of edge i, A_i is the area of edge i, and u is a positive constant. Here ψ can be any flow variable (pressure, density, total velocity, etc.). The employment of the positive exponent u has the effect of pushing the grid toward more uniformity, and guarding against overadaptation near discontinuities. An alternative gradient-based adaptation indicator is computed using

$$\varepsilon_i = \left|\Delta\left(\nabla \psi \cdot \vec{l}\,\right)_i\right| A_i^{1+u} , \tag{3.3}$$

where $\Delta\left(\nabla \psi \cdot \vec{l}\,\right)_i$ is the difference of the gradient of ψ between the two endpoints of edge i projected in the direction tangent to edge i. In the tests we performed, we found that u=1/2 gave reasonable results for most cases. We use this value of u in all cases, unless otherwise noted. Also, ε_{max} is taken to be the L_2 norm of ε over all edges, given by

$$\varepsilon_{\max} = L_2\left\|\varepsilon\right\| = \sqrt{\frac{1}{Ne}\sum_{i=1}^{Ne}\varepsilon_i^2} \ , \tag{3.4}$$

where Ne is the total number of edges in the grid. A comparison of results from the adaptation indicators given by (3.2-3.3) is given in section 4.

2. P-refinement

P-refinement, or order refinement, allows for a distribution of SVs where the degree of the polynomial reconstruction may vary from one SV to another. Unlike h-refinement, p-refinement does require significant modification of the solver itself. Among other things, the terms N and N_s in (2.6) and (2.9) are no longer constant, but depend on the level of p-refinement of the current cell. In addition, computation of the face-averaged terms in (2.13) is not as straightforward as before. For example, consider the case where a linear SV is adjacent to a quadratic SV, as shown in Figure 4. Here, the face-averaged shape functions for CV faces on SV boundaries must be computed in parts. For the corner CVs in the quadratic partition (right), the face-averaged shape functions are computed as usual, but the face-averaged shape function for the side CV must be computed in two parts to coincide with the intersection of that CV face with the face of the adjacent CV in the linear SV. With the face-averaged shape functions computed in this manner, the face-averaged terms in (2.13) can be readily computed.

Let the adaptation indicator ε_i for edge i be the same as is defined in (3.2), and ε_{max} is again taken to be the L_2 norm of ε over all edges. If for any edge i, $\varepsilon_i>\beta\varepsilon_{max}$, then the degree of polynomial reconstruction for the cells adjacent to edge i, is increased by 1. Similarly if $\varepsilon_i<\gamma\varepsilon_{max}$, then the degree of polynomial reconstruction for the cells adjacent to edge i is decreased by 1, and if $\beta\varepsilon_{max}\leq\varepsilon_i\leq\gamma\varepsilon_{max}$ the polynomial degree is left unchanged. Here $\beta,\gamma>0$ are user specified constants. In the tests we performed, $\beta=1$ and $\gamma=0.6$ gave reasonable results. In the case considered here, only one level of p-refinement is used for which β is taken to be 1.

3. Hp-refinement

For simplicity, simultaneous h- and p-refinements are carried out in a decoupled manner. H-refinement is first performed to generate a new grid, and p-refinement is then performed to increase or decrease the degree of the polynomial reconstruction for each SV in the new grid. As new SVs are created as a consequence of h-refinement, the polynomial degree is set to minimum (1 in this case), and may not be increased as a result of p-refinement. This is a safeguard to ensure that the lowest possible degree polynomial is used near very high gradient regions. Such a measure should minimize oscillations due to extreme flow phenomena such as shock waves. This methodology for hp-refinement should be able to tackle a wide range of problems, resolving both shock waves and fine smooth features simultaneously. This is in contrast to another recent approach by Remacle et al. [20], where both h- and p-refinements are carried out in the same regions. While this approach may work well for some situations, it could lead to large oscillations for problems involving strong shock waves. This is due to the fact that there is no mechanism in place to prevent the use of a high-order polynomial near a shock wave, other than a limiting procedure.

4. Numerical Tests

In this section, the SV method with local adaptive hp-refinement is evaluated for the 2D Euler equations. Several well known inviscid flow test cases are utilized to demonstrate the effectiveness of local hp-refinement. In all cases involving shock waves, the TVD limiter presented in Harris et al. [14] is employed to maintain a stable numerical scheme. In all cases involving curved-wall boundaries, the approach of Krivodonova and Berger [18] is utilized to maintain low computational cost. This approach was successfully implemented for the SV method in Harris et al. [14]. All of the following cases employ the Rusanov [22] flux, and for time integration we use either the 2^{nd} or 3^{rd} order Strong Stability-Preserving [12] (SSP) Runge-Kutta scheme.

1. Subsonic and transonic flow over NACA 0012 airfoil

As a demonstration of the p-refinement technique, subsonic flow at Mach=0.4, and angle of attack of 5^{o} around a NACA 0012 airfoil is considered. The grid used for the NACA 0012 case is semi-structured, as shown in Figure 5. The outer boundary is 20 chord lengths away from the center of the airfoil. For this case, the SVs near the farfield are orders-of-magnitude larger than the SVs near the airfoil surface. The adaptation indicator given in (3.2) is selected for this problem, with the exponent u taken to be zero. The choice of exponent for this case was made after many numerical experiments showed that a positive area weighting produced significant adaptation near the farfield boundary, which is not necessary. Also, ψ in (3.2) is taken to be the Mach number.

As a test of the p-refinement technique, a converged solution from a 2nd order simulation is subjected to 1 level of p-refinement and run until convergence. This case will be subsequently denoted as the 2-3 case. Thus, the resulting solution will contain some 2nd order SVs and some 3rd order SVs. Mach contours for this simulation, as well as uniform 2nd and 3rd order simulations for comparison, are shown in Figure 6. Figure 6d shows Mach contours for the 2-3 case and for a uniform 3rd order case for comparison. It is evident that Mach contours for the 2-3 case agree reasonably well with the 3rd order contours, and the large errors present near the airfoil in the 2nd order case are eliminated in the 2-3 case. The convergence history for this case is shown in Figure 7a. It is apparent that the 2-3 case costs slightly more than the 2nd order case in terms of required time steps, but it costs much less than the 3rd order case. This is encouraging, as the 2-3 case agrees with the 3rd order case extremely well at the airfoil surface (which is where a lift/drag calculation would take place), for significantly less computational cost than that required for a full 3rd order simulation. Figure 7b clarifies which SVs are increased to 3rd order for the 2-3 case. It is clear that the majority of SVs in the domain are still 2nd order, and 3rd order SVs are only used in regions of largest change in Mach number.

As a demonstration of the h-refinement technique, transonic flow at Mach=0.9, and angle of attack of 1° around a NACA 0012 airfoil is considered. The base grid used for this simulation is the same as that used for the above subsonic case. Here the adaptation indicator (3.2) is computed based on density and total energy, and again the exponent u is taken to be zero to avoid unnecessary refinement in the farfield. This case involves shock waves on both the upper and lower surface of the airfoil, so the aforementioned TVD limiter is utilized to maintain stability. For this case, the value α=2.5 gave reasonable results, while lower values of α tended to over-adapt in regions far away from the shock waves. A converged 2nd order solution is again taken as the initial condition, and grid is then re-adapted 3 times and then frozen for the remainder of the simulation.

Figures 8 and 10 show the computational grids and Mach contours, respectively, for 1-4 levels of adaptive h-refinement. It is evident that without refinement, the shock waves are smeared over several grid cells and the solution is of low quality. As the adaptation level is increased, the grid density in the vicinity of both shock waves and expansions is increased markedly. This produces a much higher quality solution with more precisely captured and finely resolved shock waves.

2. Mach 3 wind tunnel with a step

This problem was studied extensively by Woodward and Colella [34], and has been widely used to assess the performance of shock-capturing methods. The 2D wind tunnel is 3 units long and 1 unit wide, with a step of 0.2 units high located at 0.6 units from the tunnel inlet. The initial condition is a Mach 3 right-going uniform flow. Inviscid wall boundary conditions (reflective) are used for tunnel wall boundaries, while inflow and outflow boundary conditions are used at the inlet and exit of the wind tunnel. It is well known that the corner of the step is a singularity, and often leads to a spurious Mach stem at the downstream bottom wall, and an erroneous entropy layer at the bottom wall. In Woodward and Colella [34], various numerical treatments were used to remedy these artifacts. In the present study, no special treatments were used for the singularity to see how the singularity affects the numerical solutions.

Both 2nd and 3rd order simulations are carried out, using various levels of h-refinement. Figure 10 shows a comparison of results using the adaptation indicators (3.2-3.3) for a 3rd order simulation with 1 level of refinement. It is apparent that the results are very similar, while (3.3) is more expensive to compute than (3.2). In addition, as the number of adaptation levels is further increased, (3.3) becomes extremely sensitive, and as a result, further adaptation becomes increasingly non-isotropic. For this reason, and because it is significantly less expensive to compute while producing desirable results, we use the adaptation indicator (3.2) which is computed based on density, and the area weighting exponent u=1/2. The value of α is taken to be 1. The Figures 11-12 show grids and density contours obtained for a 2nd order simulation with 0-3 levels of h-refinement. All plots show 30 even contours of density between 0.09 and 4.53. It is clear that as the adaptation level is increased, the grid becomes exceedingly dense in the vicinity of the shock wave, near the corner of the step, and downstream of the triple point. Also as the adaptation level is increased, the shock is captured more accurately with less smearing, and the spurious Mach stem downstream of the step is reduced in size to the extent that it is barely discernible. Figures 13-14 show similar results for a 3rd order simulation. In both 2nd and 3rd order cases, the spurious Mach stem is completely eliminated for 2 or more levels of h-refinement, and when compared to global refinement, even only 1 level of h-refinement produces a much better solution with far fewer degrees of freedom than that on a grid that has been globally refined 1 level.

3. Rayleigh-Taylor instability problem

The Rayleigh-Taylor instability (RTI) problem involves a cold fluid overlying a warm fluid. Two inviscid fluids are initially taken to be in hydrostatic equilibrium in an isolated chamber, as shown in Figure 15a. The chamber is 1 unit high, and 0.25 units wide. The upper half of the chamber contains a fluid of density two, while the lower half of the chamber contains a fluid of unit density. The initial pressure field is chosen to ensure hydrostatic equilibrium, and an initial perturbation of the velocity field triggers the instability.

The flow is governed by the Euler equations with the addition of source terms in the y-momentum and energy equations which correspond to unit gravity in the downward direction. The initial data is summarized in Table I, where M_0=0.1, τ=6, γ=1.4, $\varepsilon_y = M_0\sqrt{\gamma/2}$, and $\varepsilon_x = -\varepsilon_y \tau/16$. A perturbation is selected which gives rise to a single mode instability, and inviscid wall boundary conditions are used for the chamber walls. While there are no shock waves in this problem, there is a contact discontinuity between the two fluids. Here the adaptation indicator (3.2) is computed based on density, and the values of u and α are taken to be 1/2 and 1, respectively.

Figure 16 shows 1st, 2nd, 3rd, and 4th order results for this case on both symmetric and asymmetric grids with no adaptation. In all plots, 30 even contours of density between 0.84 and 2.4 are presented. In addition, Roe flux is used for all RTI cases. From Figure 16, it is evident that as the polynomial order is increased on a uniform grid, the solution contours are over-dissipated by the limiter. Thus, if a local min/max-based limiter is used for this problem, adaptive h-refinement is essential if high-order accuracy is sought. For comparison, Figure 17 shows 2nd and 3rd order results using uniformly refined grids. Results and grids for this case obtained using adaptive h-refinement are shown in Figures 18-20. Both symmetric and asymmetric base grids are employed for this simulation. It is immediately apparent that the behavior of the RTI problem is heavily dependent on the grid used. Namely, if the initial grid is symmetric, the solution tends to stay symmetric (until numerical round-off eventually leads to asymmetries), otherwise the solution is completely asymmetric. In all cases, the typical mushroom-cap behavior is observed, with increasingly complicated flow structure downstream as the number of adaptation levels is increased. Comparing Figures 17-19, it is clear that local adaptive h-refinement is far more effective than global refinement at resolving the flow features for this problem. In fact, a much more highly resolved solution is obtained using local h-refinement with far fewer degrees-of-freedom than is necessary for a global refinement strategy to produce similar results.

4. Reflection of Mach 3 shock wave from 2 offset circular cylinders

This problem involves a right-moving Mach 3 shock wave impacting two offset circular cylinders. The domain is 1 unit high and 1 unit wide, with two 0.15 radius cylinders located at (0.4, 0.25) and (0.5, 0.75), respectively. The shock wave is initially located at x=0.2, and the solution is carried out until time=0.16. Here the adaptation indicator (3.2) is computed based on density, and the values of u and α are taken to be 1/2 and 1, respectively.

The base grid for this case, and results for 2nd, 3rd and 4th order simulations with no adaptation are shown in Figure 21. It is evident that the 3rd order simulation has more effective resolution of the shock waves than the 2nd order simulation, however, the 4th order simulation is not more resolved than the 3rd order simulation. This is likely because limiters bases on a local maximum principle are often over dissipative, and can effectively reduce a high-order simulation to low-order.

Figures 22-23 show 2nd and 3rd order results and grids for this simulation subjected to various levels of h-adaptation. In all plots, 30 even contours of density between 0.3 and 18.0 are presented. It is apparent that as the adaptation level is increased, the resolution of the shock waves increases markedly. This is true for the region where the shock reflects off of the cylinder, as well as for the region where the shocks intersect. From Figure 23, it is clear that the 3rd order simulation gives better resolution of the shocks, and more accuracy in smooth regions than the 2nd order case.

5. Conclusions

The high-order quadrature-free spectral volume method has been successfully extended for use with local adaptive hp-refinement. A hierarchical edge-based adaptation algorithm was employed for high efficiency. The p-refinement methodology was effectively utilized for the case of subsonic flow over a NACA 0012 airfoil, and the h-refinement technique was also employed with success for transonic flow over a NACA 0012 airfoil. In addition, the h-refinement technique was also demonstrated for supersonic flow in a wind tunnel with a forward-facing step, reflection of a moving shock wave off of 2 offset circular cylinders, and the Rayleigh-Taylor instability problem. It was demonstrated that adaptive h-refinement is far more effective than global refinement at resolving important flow features, and a much more highly resolved solution can often be obtained using adaptive h-refinement with far fewer degrees-of-freedom than is necessary for a global refinement strategy to produce similar results. The extension of the adaptive quadrature-free SV method for use with implicit solvers for the Euler and Navier-Stokes equations will be the subject of future research.

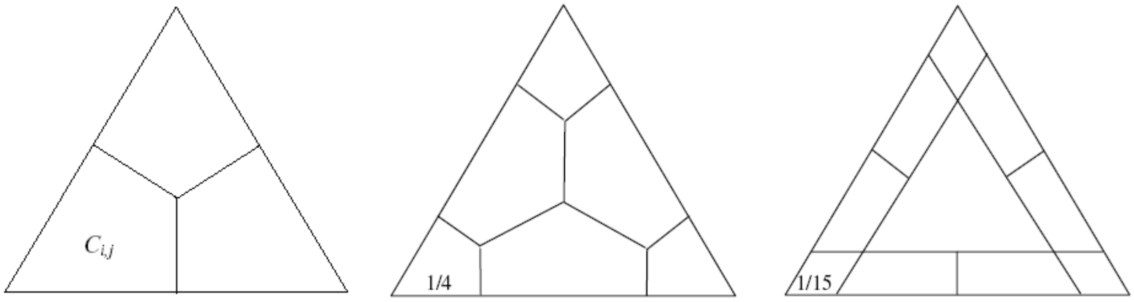

(a) (b) (c)

Figure 1. Partitions of a triangular SV supporting linear, quadratic and cubic data reconstructions, shown in (a), (b) and (c), respectively.

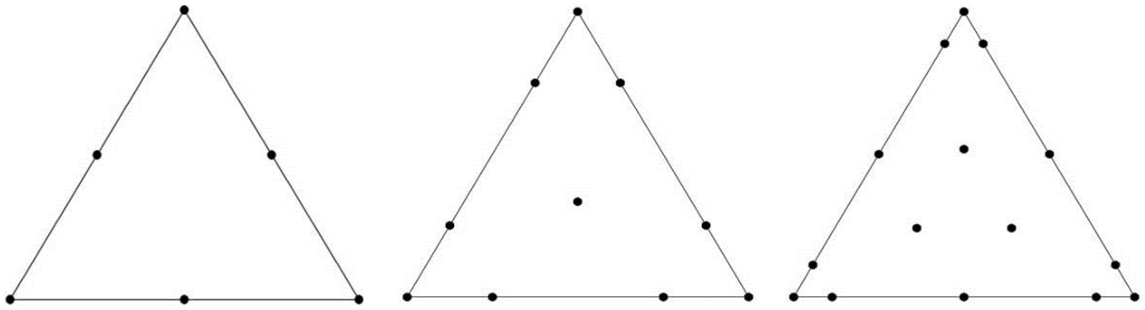

(a) (b) (c)

Figure 2. Nodal sets in a triangular SV supporting quadratic, cubic and quartic data reconstructions for the flux vector, shown in (a), (b) and (c), respectively.

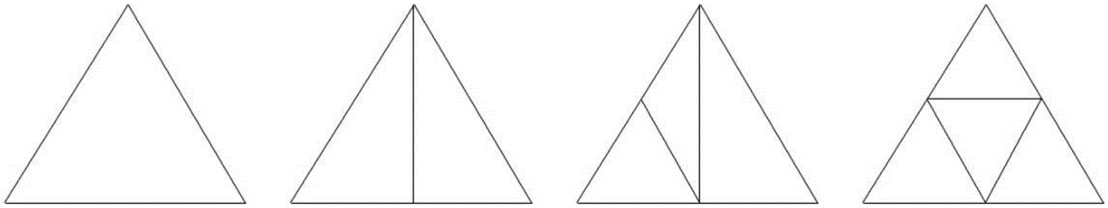

(a) (b) (c) (d)

Figure 3. Four situations that can occur when a SV is refined; (a) No edges are split so the SV is unchanged; (b) Two new SVs are generated due to one split edge; (c) Three new SVs are generated due to two split edges; (d) Four new SVs are generated due to three split edges.

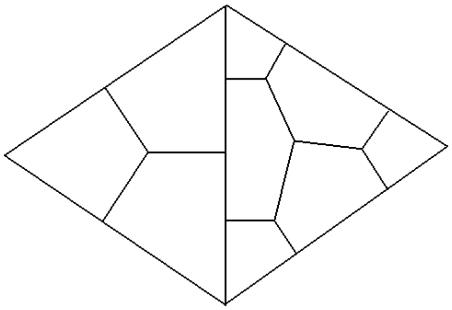

Figure 4. Two adjacent SVs with p-refinement levels differing by one. The left SV contains a linear partition, and the right SV contains a quadratic partition.

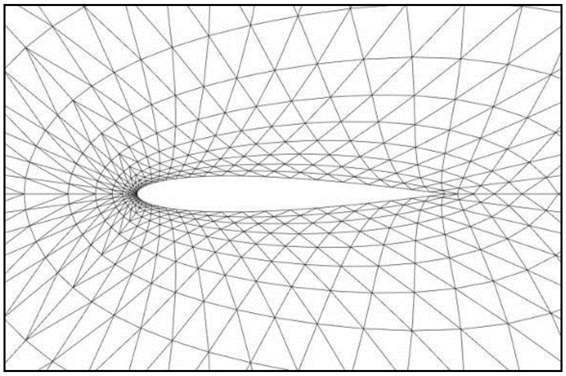

Figure 5. Base grid for subsonic and transonic flow over NACA 0012 airfoil (48x16x2 triangles).

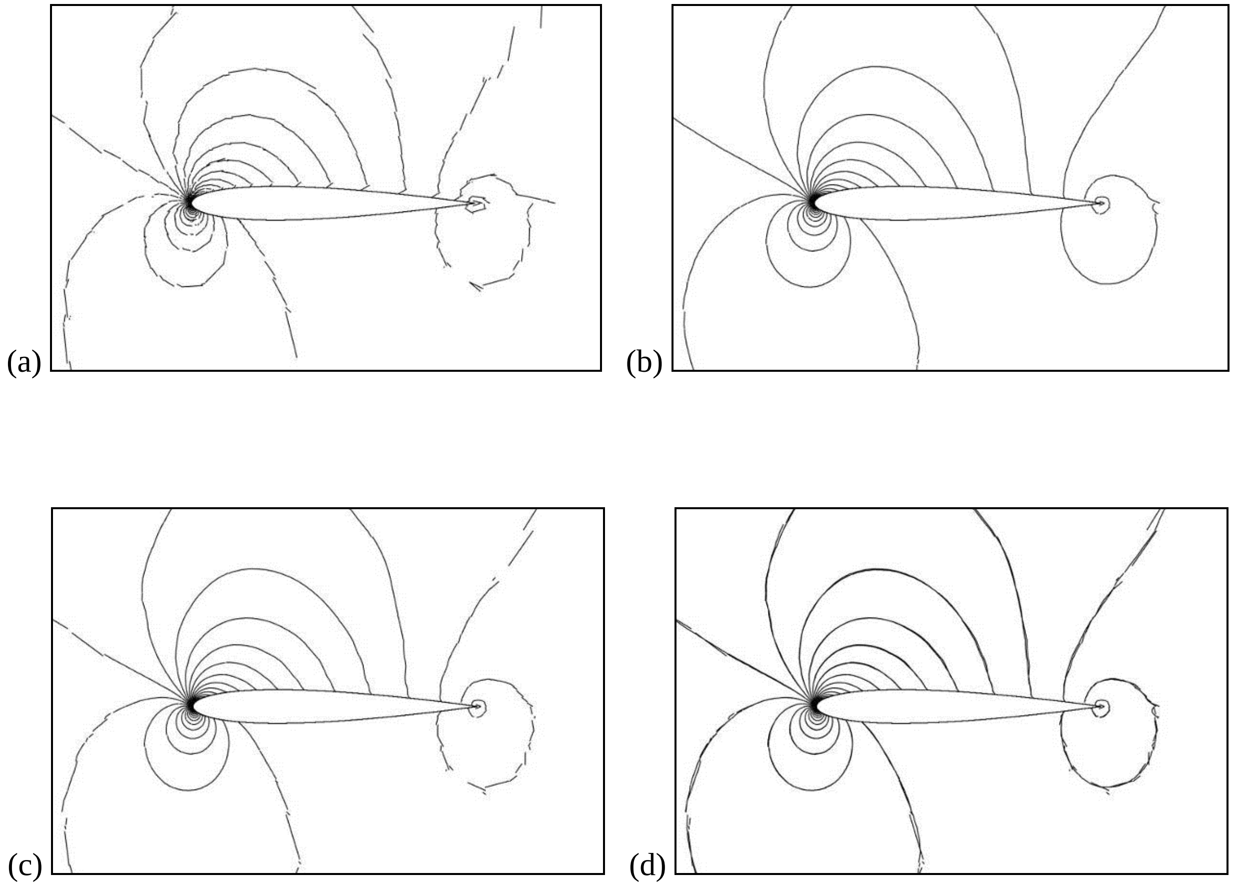

Figure 6. Contours of Mach number for subsonic flow over a NACA 0012 airfoil; (a) 2nd order (4,608 DOFs); (b) 3rd order (9,216 DOFs); (c) 1 level of p-adaptation starting from the converged 2nd order solution shown in (a) (6,519 DOFs); (d) The 1 level case shown with the 3rd order case to illustrate differences.

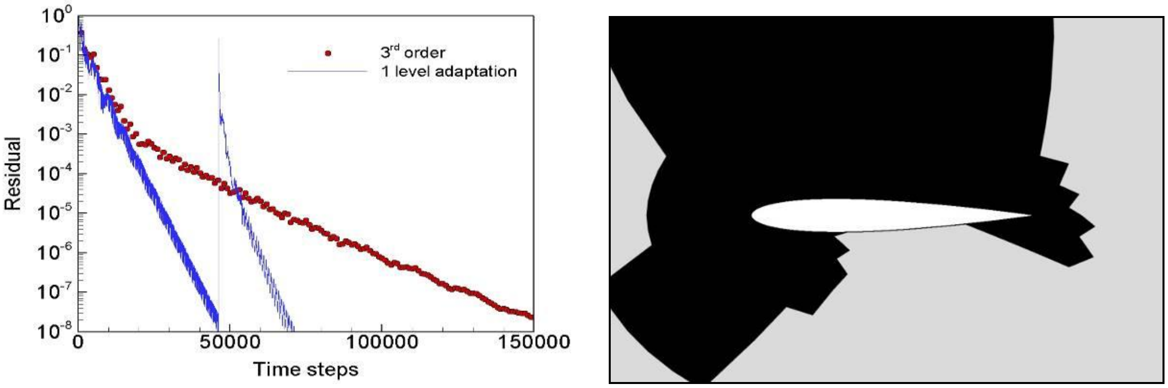

(a) (b)

Figure 7. Results for subsonic flow over NACA 0012 airfoil (a) Convergence history (The red circles are for a uniform 3rd order case, while the blue line shows the convergence of the 2nd order solution, the p-adaptation step, and the convergence of the resulting “2-3” case) (b) Schematic showing the status of p-refinement after refining from a converged 2nd order solution. Black regions represent 3rd order SVs, while gray regions represent 2nd order SVs.

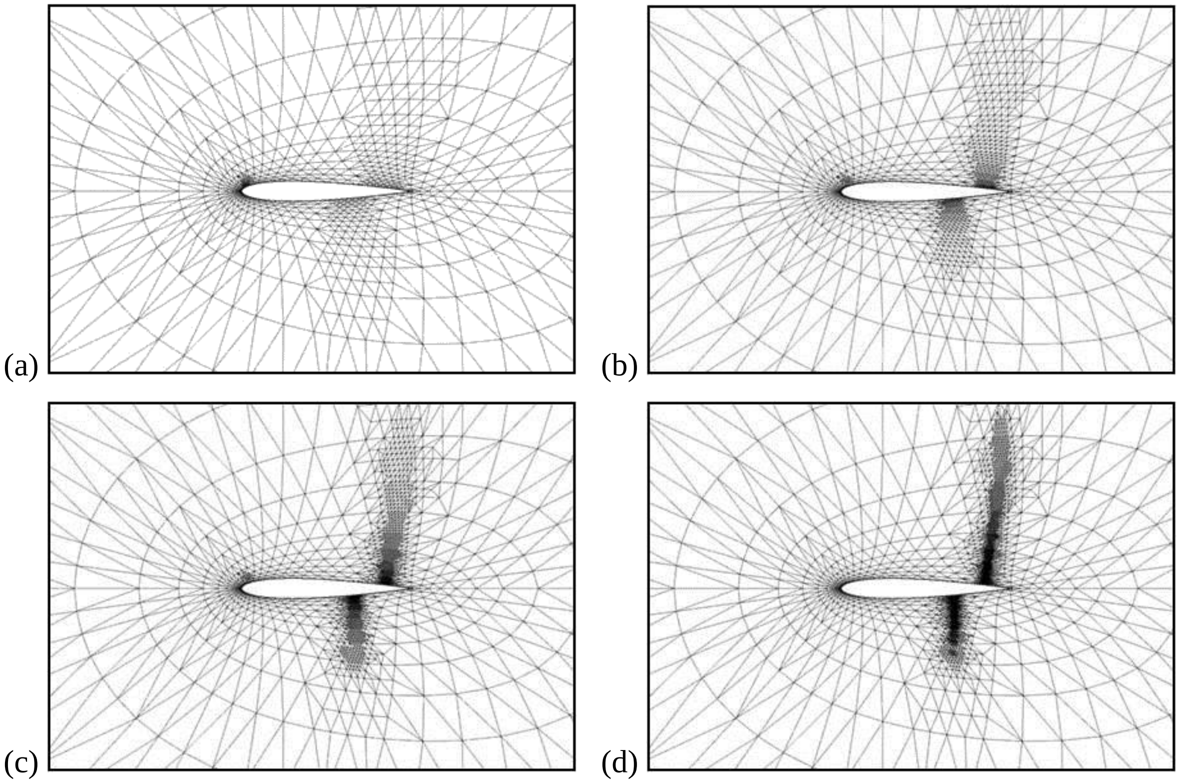

Figure 8. Grids for 2nd order solution of transonic flow over NACA 0012 airfoil with adaptive h-refinement; (a) 1 level (3,349 triangles); (b) 2 levels (9,337 triangles); (c) 3 levels (30,498 triangles); (d) 4 levels (92,551 triangles); A converged 2nd order solution on the base grid is used as the initial condition for all cases. The grid is re-adapted 3 times (once every 100 time steps for the first 300 time steps), and then frozen for the remainder of the simulation.

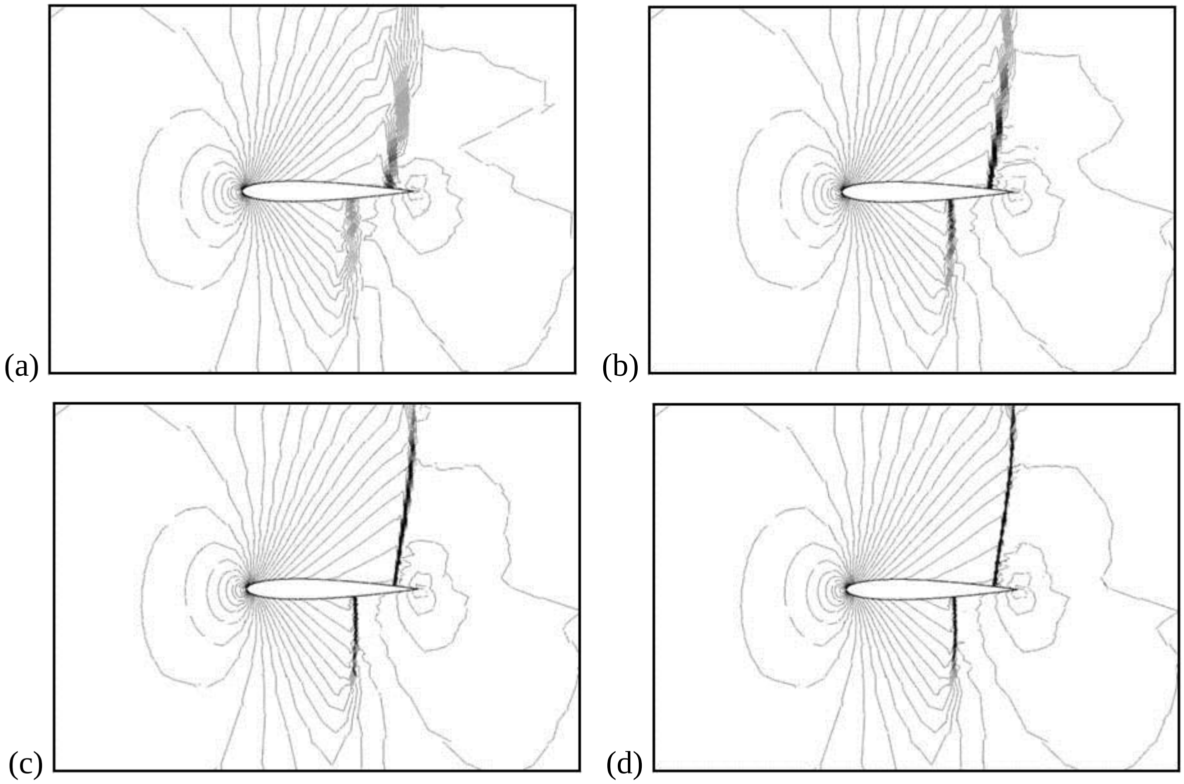

Figure 9. Mach contours for 2nd order solution of transonic flow over NACA 0012 airfoil with adaptive h-refinement; (a) 1 level (10,047 DOFs); (b) 2 levels (28,011 DOFs); (c) 3 levels (91,494 DOFs); (d) 4 levels (277,653 DOFs); A converged 2nd order solution on the base grid (Figure 5a) is used as the initial condition for all cases.

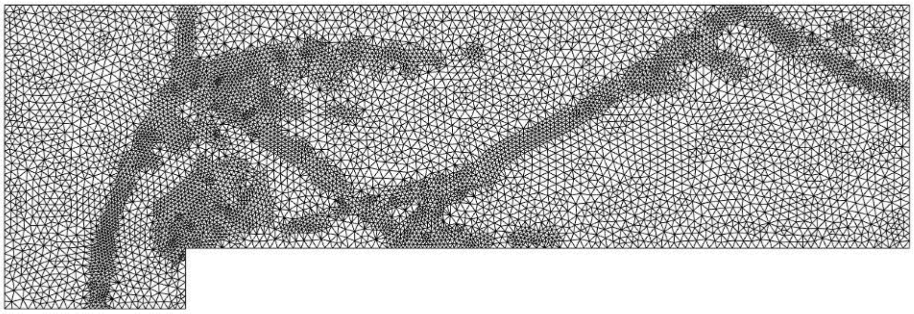

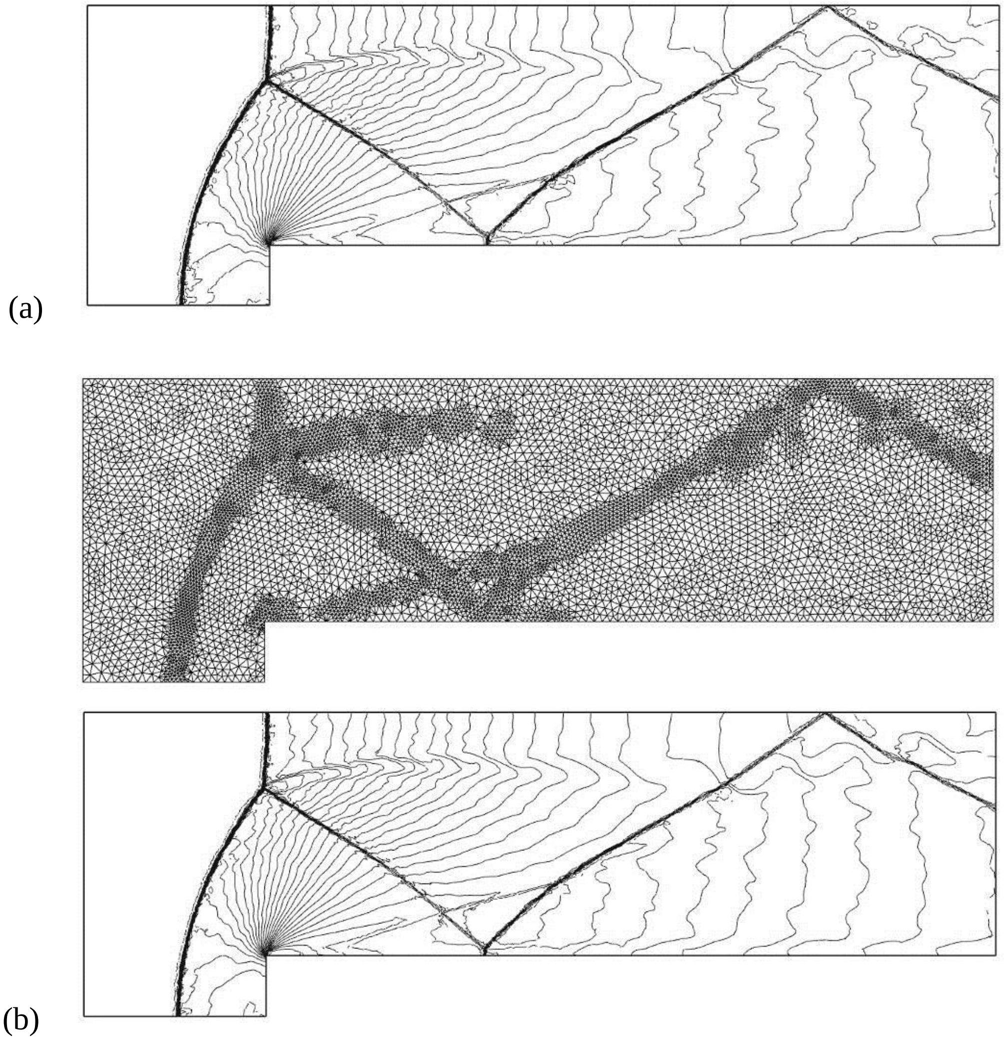

Figure 10. Grid and density contours for 3rd order SV scheme under 1 level of adaptive h-refinement at time=4.0; (a) Using adaptation indicator given by (3.2) (89,928 DOFs); (b) Using adaptation indicator given by (3.3) (84,228 DOFs); Refined from base grid every 100 time steps.

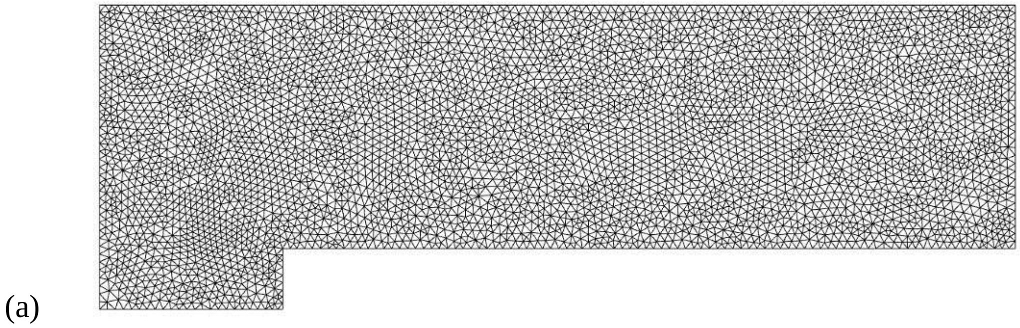

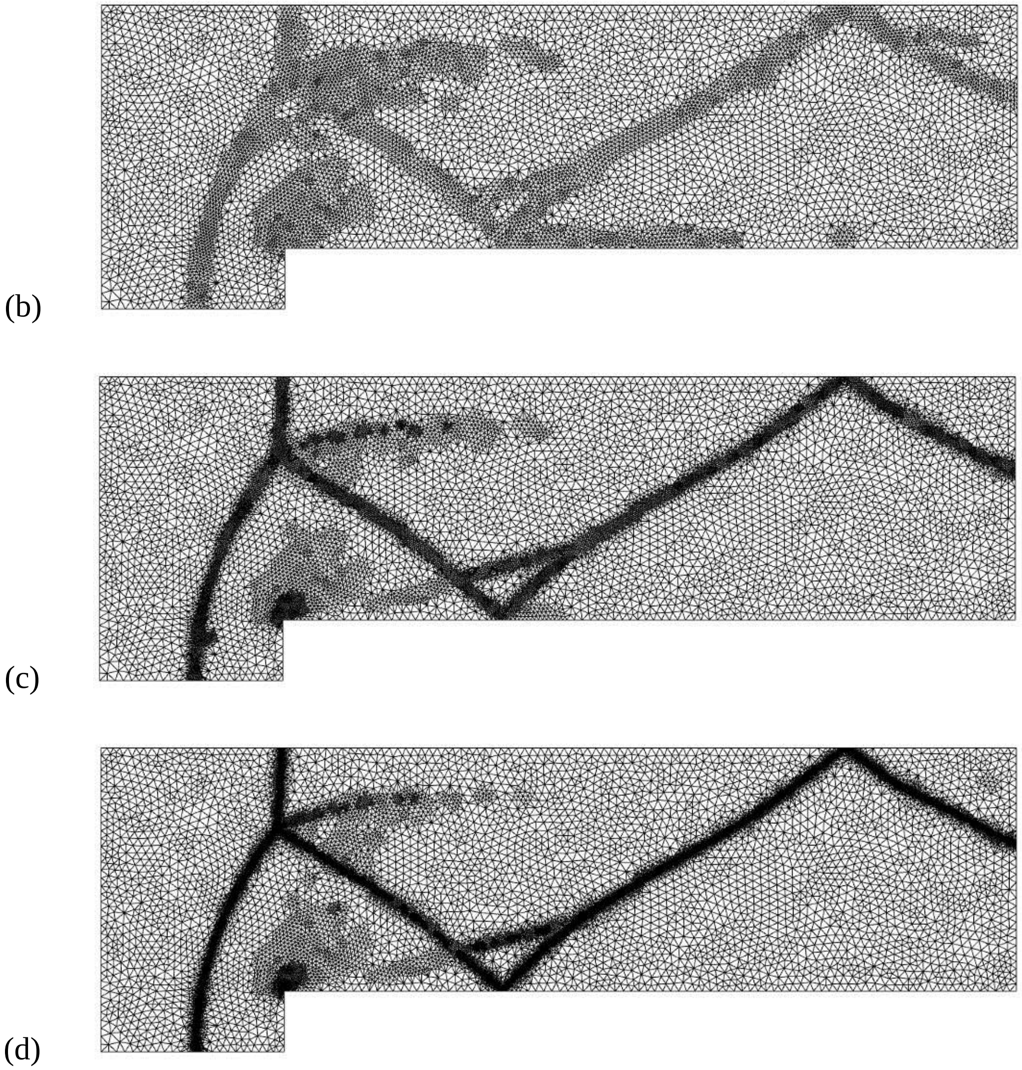

Figure 11. Grids for 2nd order SV scheme under adaptive h-refinement at time=4.0; (a) Base grid (8,746 triangles); (b) 1 level (14,765 triangles); (c) 2 levels (22,104 triangles); (d) 3 levels (35,846 triangles); Refined from base grid every 100 time steps.

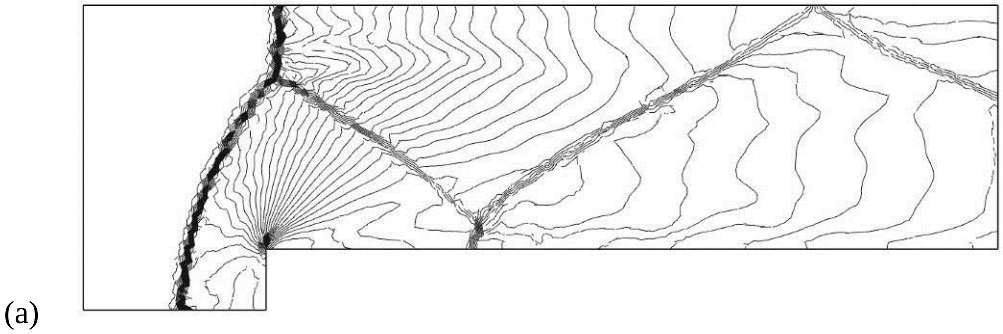

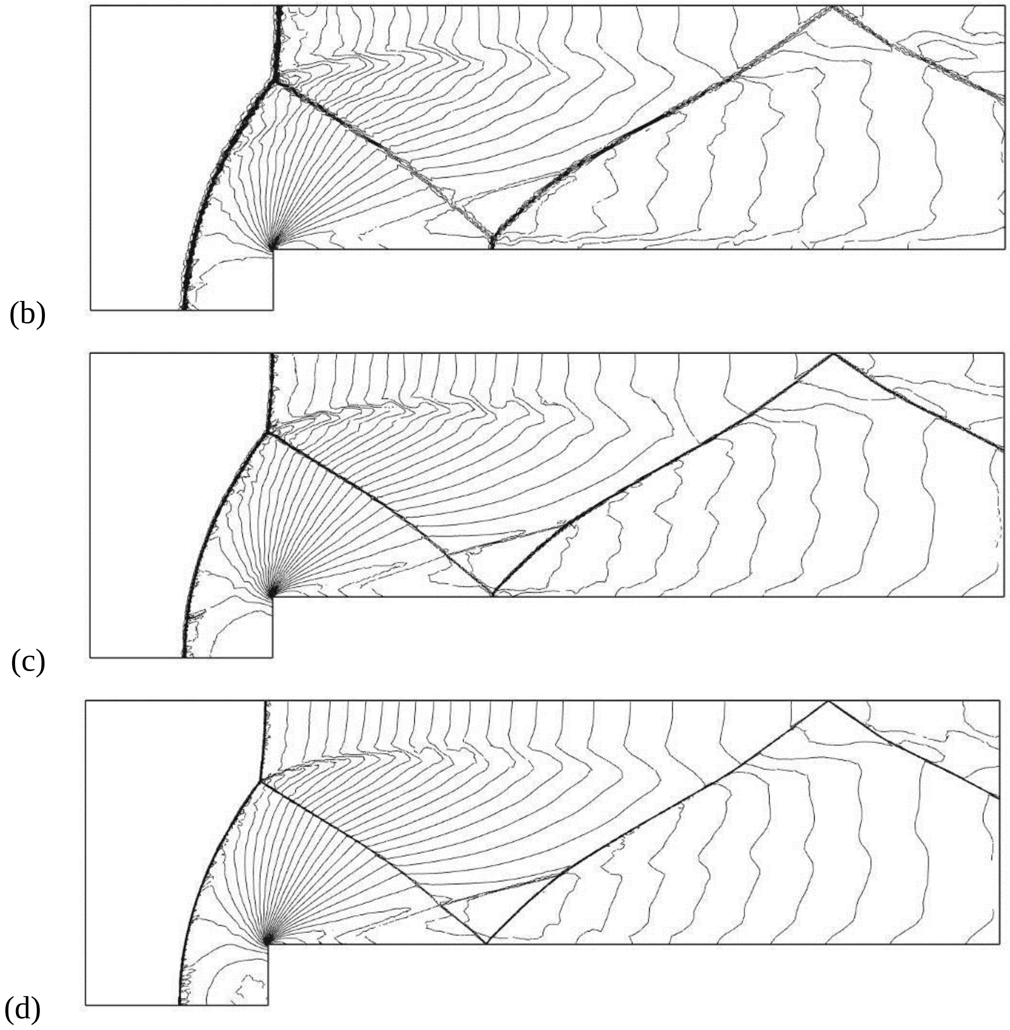

Figure 12. Density contours for 2nd order SV scheme under adaptive h-refinement at time=4.0; (a) Base grid (26,238 DOFs); (b) 1 level (44,295 DOFs); (c) 2 levels (66,312 DOFs); (d) 3 levels (107,538 DOFs); Refined from base grid every 100 time steps.

(a)

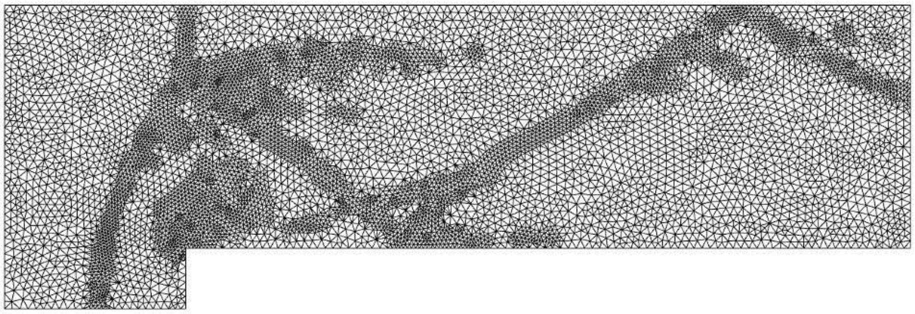

(b)

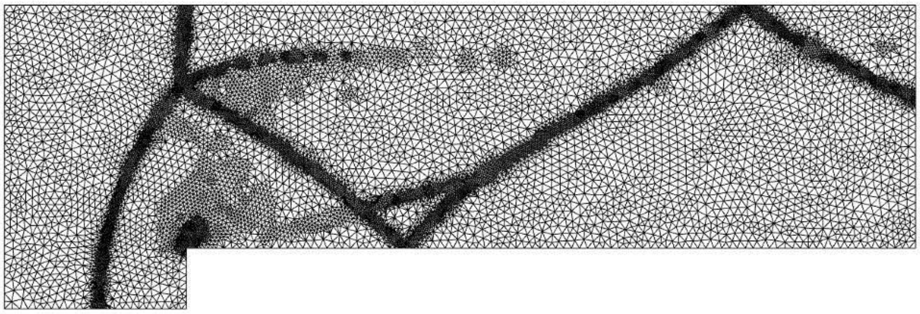

Figure 13. Grids for 3rd order SV scheme under adaptive h-refinement at time=4.0; (a) 1 level (14,988 triangles); (b) 2 levels (22,677 triangles); Refined from base grid every 100 time steps.

(a)

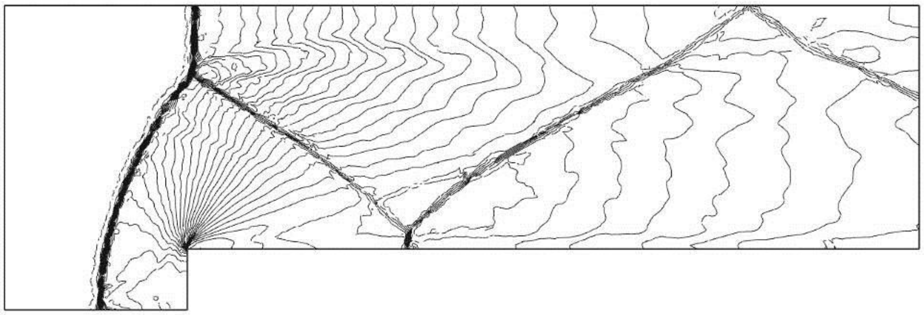

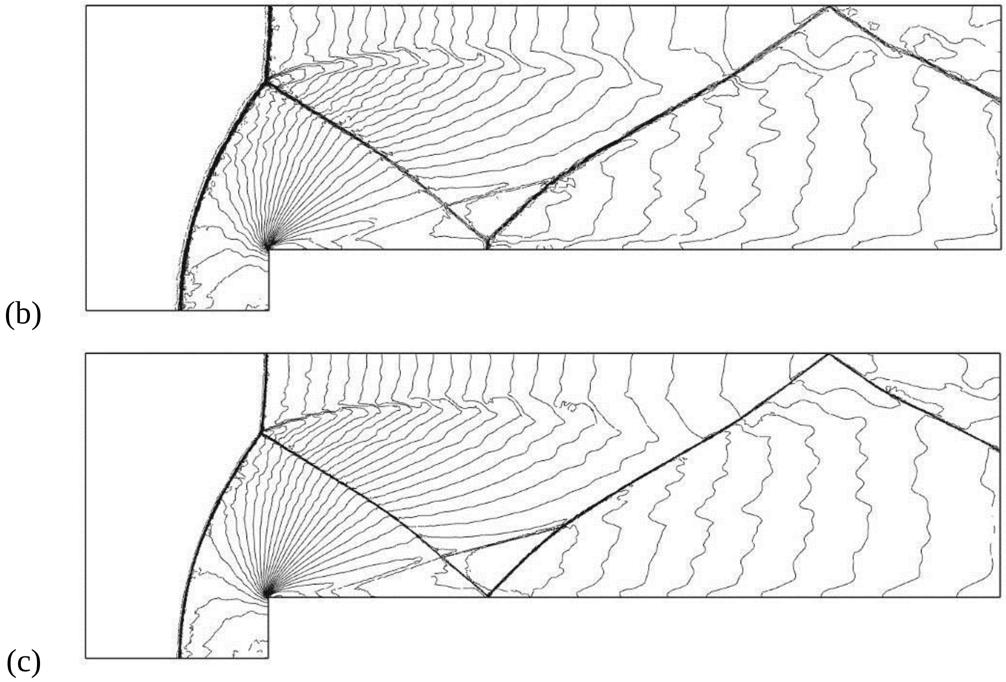

Figure 14. Density contours for 3rd order SV scheme under adaptive h-refinement at time=4.0; (a) Base grid (52,476 DOFs); (b) 1 level (89,928 DOFs);(c) 2 levels (136,062 DOFs); Refined from base grid every 100 time steps.

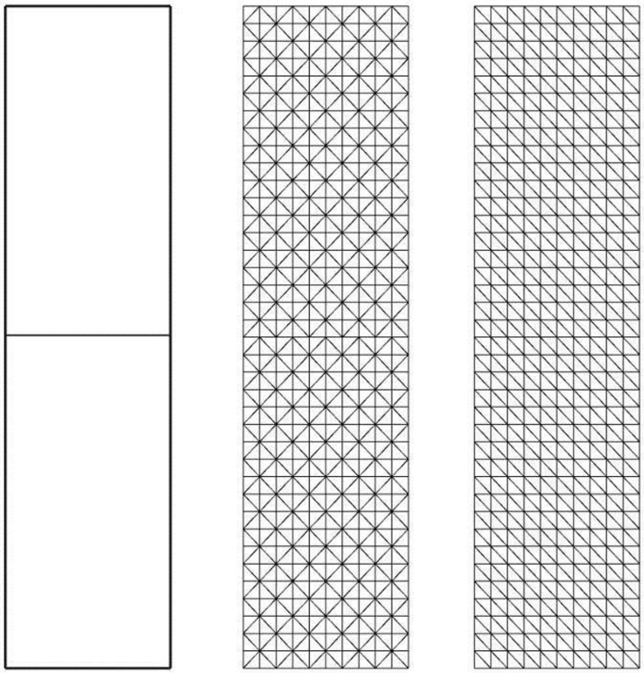

Figure 15. Problem domain and grids for RTI problem; (a) domain; (b) symmetric grid (10x38x2 triangles); (c) asymmetric grid (10x38x2 triangles).

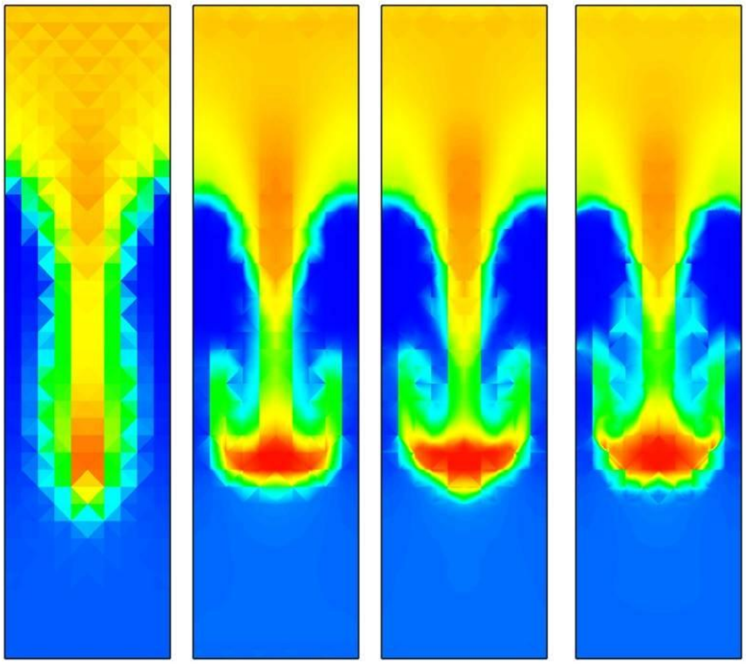

(a)

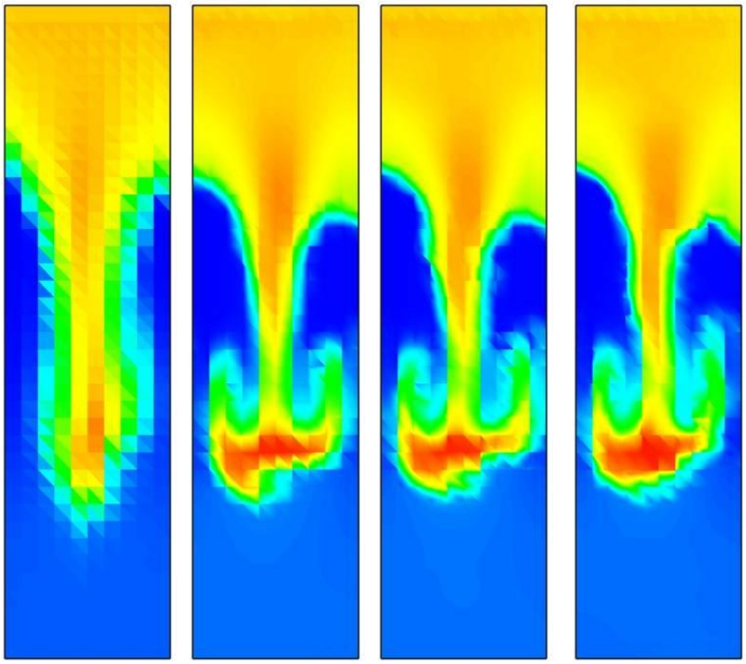

(b)

Figure 16. 1st, 2nd, 3rd, and 4th order density contours (left-to-right, 760, 2,280, 4,560, and 7,600 DOFs) for RTI problem at time=1.8 with no adaptation; (a) symmetric grid; (b) asymmetric grid.

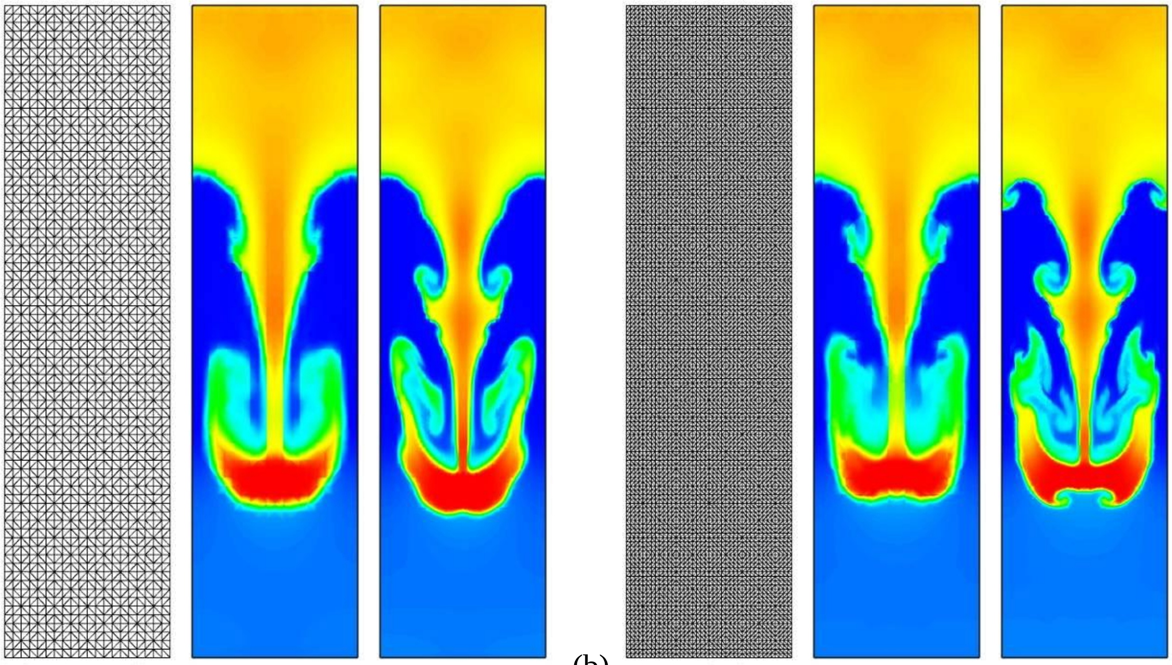

(a) (b)

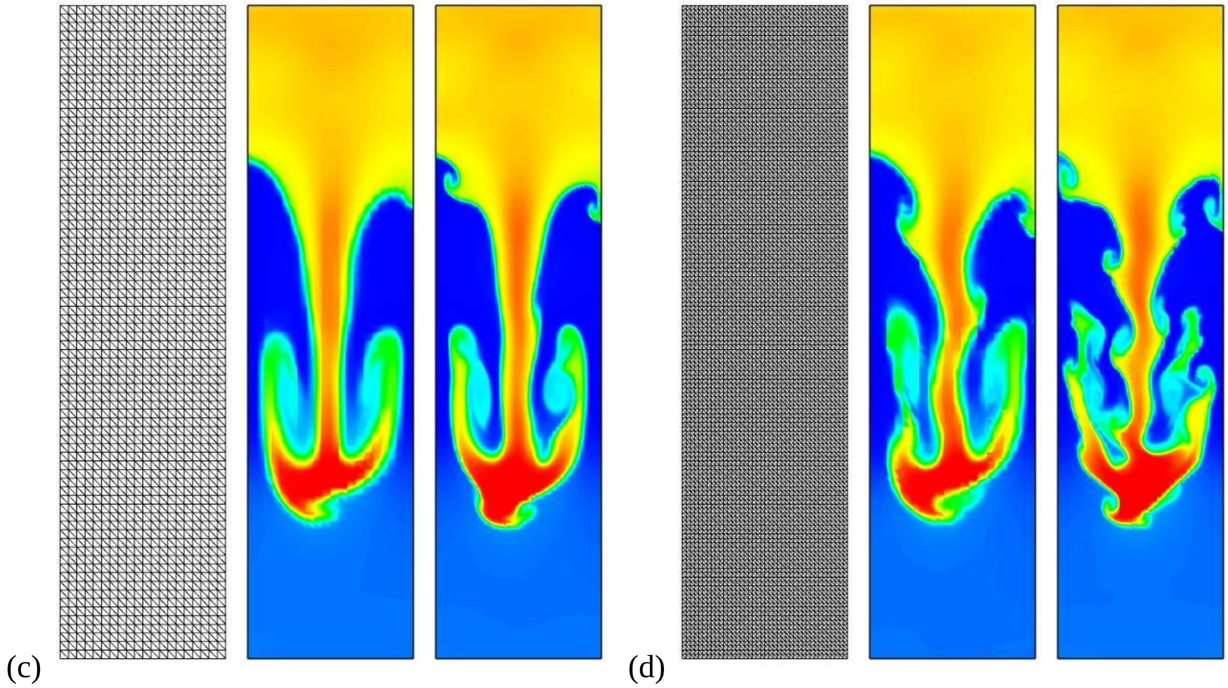

Figure 17. Grid, 2nd and 3rd order density contours (left-to-right) for RTI problem at time=1.9 with no adaptation; (a) symmetric grid (20x76x2 triangles); (b) symmetric grid (40x152x2 triangles); (c) asymmetric grid (20x76x2 triangles); (d) asymmetric grid (40x152x2 triangles).

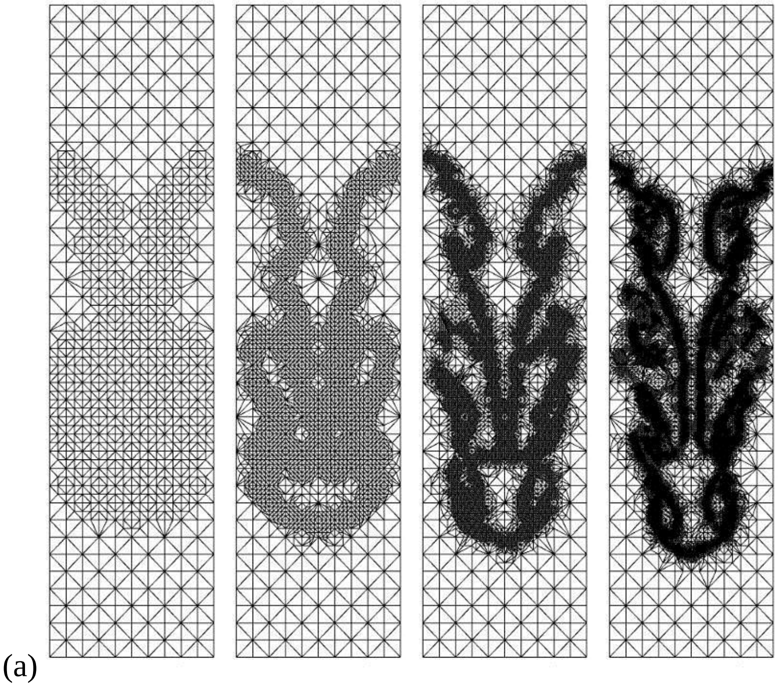

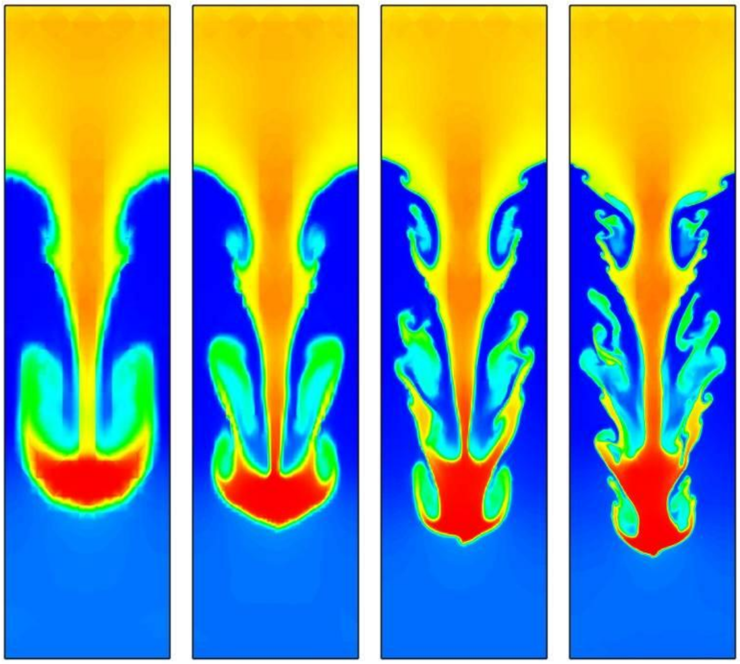

(b)

Figure 18. Results for RTI problem at time=1.9 on symmetric grids; (a) grids obtained using 1-4 levels of adaptation (left-to-right, 1,810, 4,960, 14,079, and 38,281 triangles); (b) 2nd order density contours obtained using 1-4 levels of adaptation (left-to-right, 5,430, 14,880, 42,237, and 114,843 DOFs); Refined from base grid every 10 time steps.

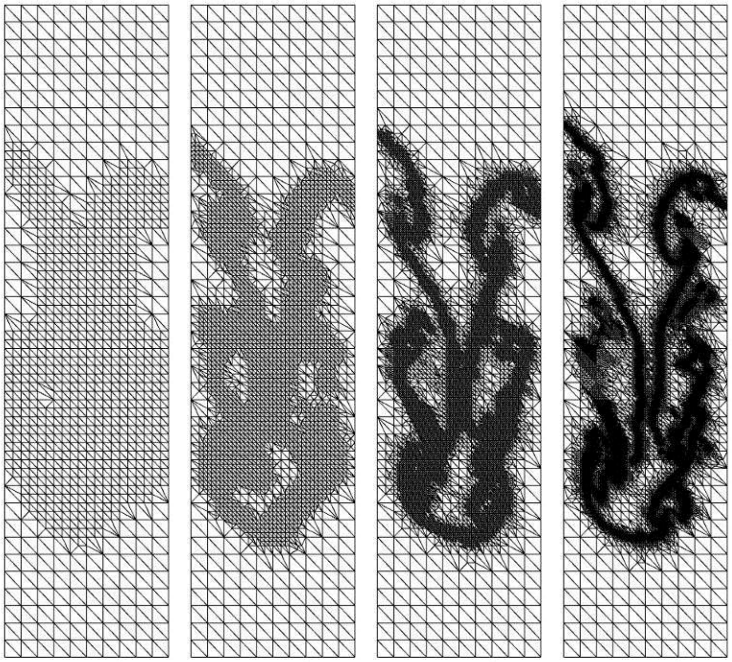

(a)

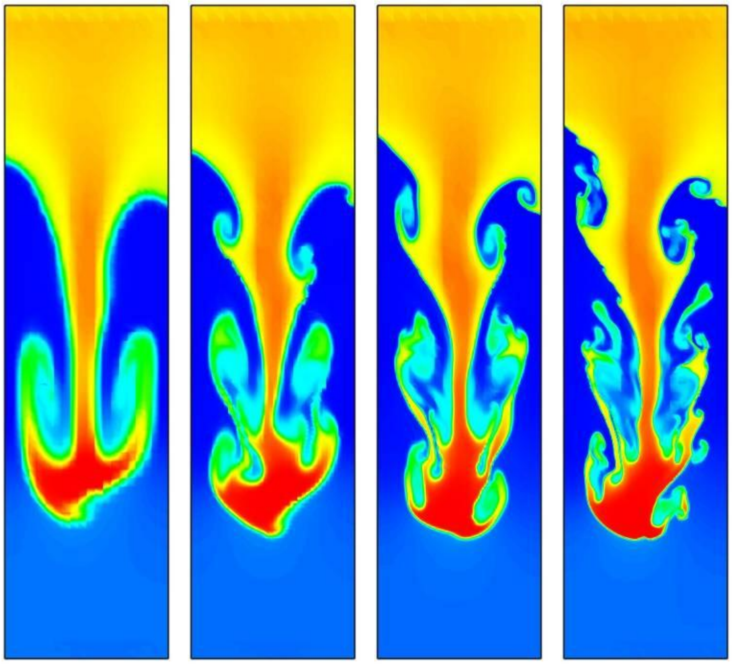

(b)

Figure 19. Results for RTI problem at time=1.9 on asymmetric grids; (a) grids obtained using 1-4 levels of adaptation (left-to-right, 1,834, 5,226, 14,391, and 36,185 triangles); (b) 2nd order density contours obtained using 1-4 levels of adaptation (left-to-right, 5,502, 15,678, 43,173, and 108,555 DOFs); Refined from base grid every 10 time steps.

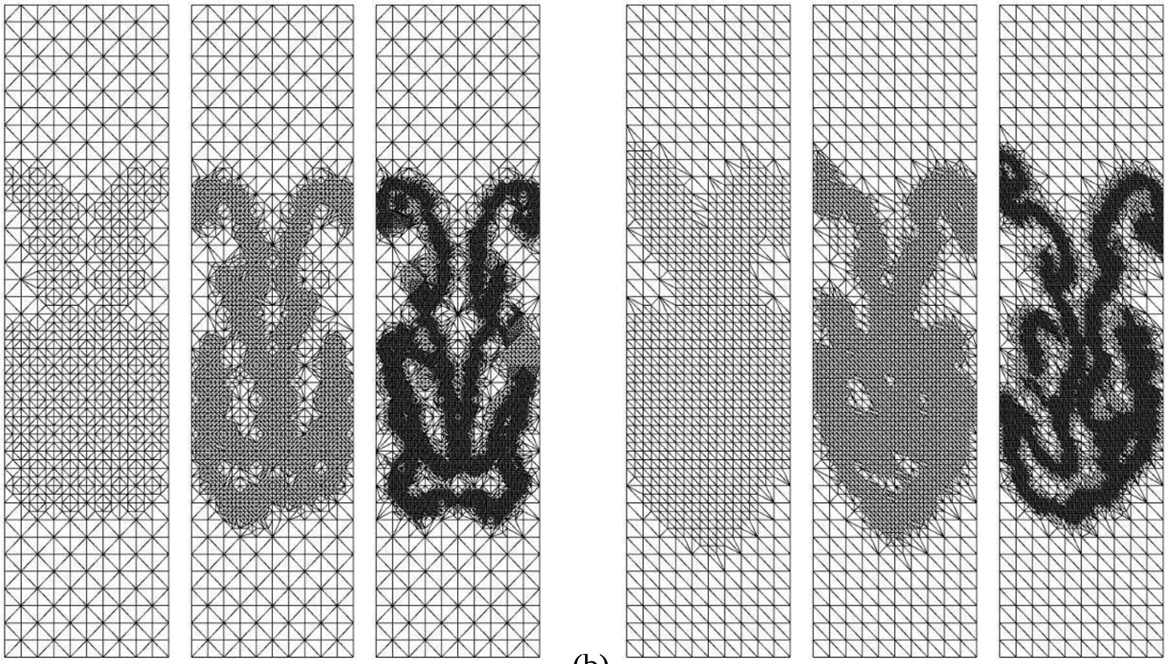

(a) (b)

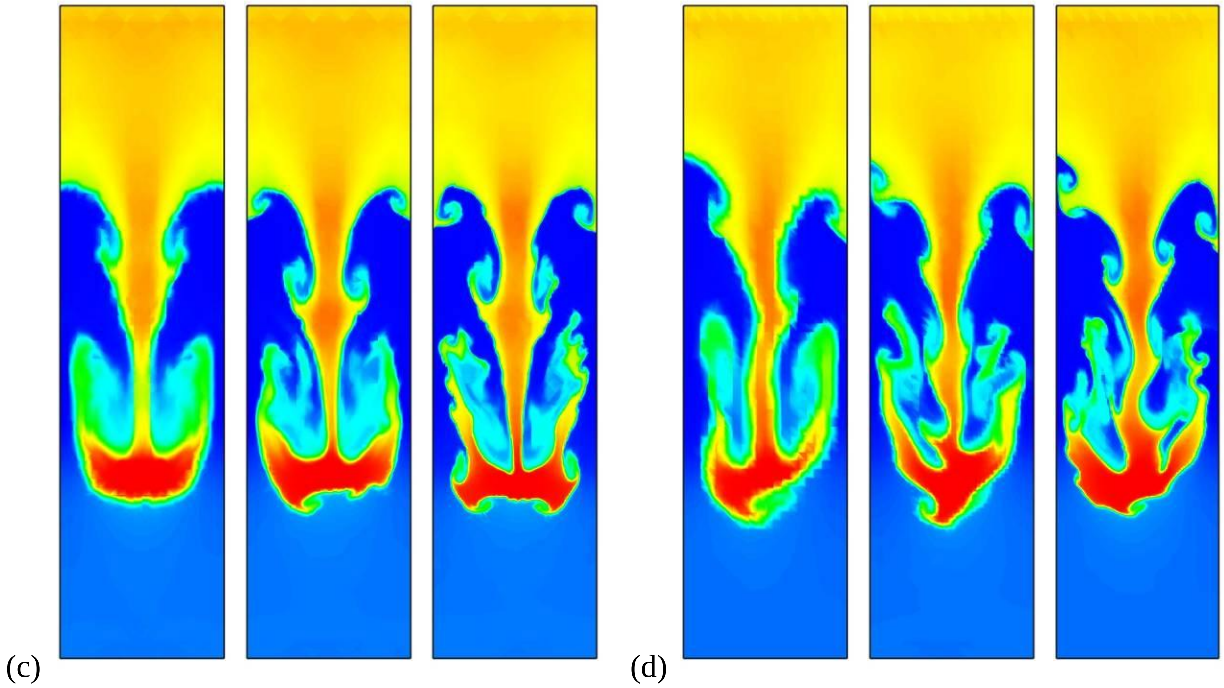

Figure 20. 3rd order results for RTI problem at time=1.9 obtained using 1-3 levels of adaptation; (a) symmetric grids (left-to-right, 1,770, 4,788, and 13,513 triangles); (b) asymmetric grids (left-to-right, 1,891, 5,254, and 13,698 triangles); (c) density contours for symmetric grids (left-to-right, 10,620, 28,728, and 81,078 DOFs); (d) density contours for asymmetric grids (left-to-right, 11,346, 31,524, and 82,188 DOFs); Refined from base grid every 10 time steps.

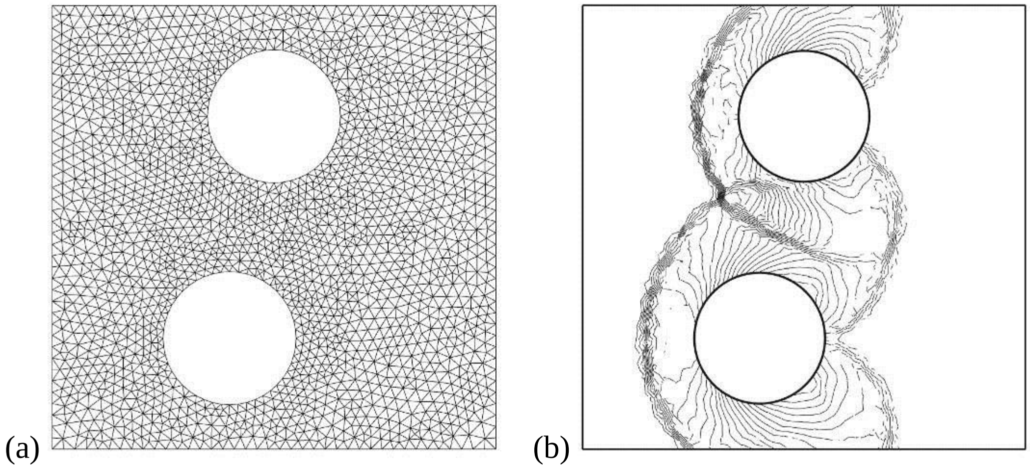

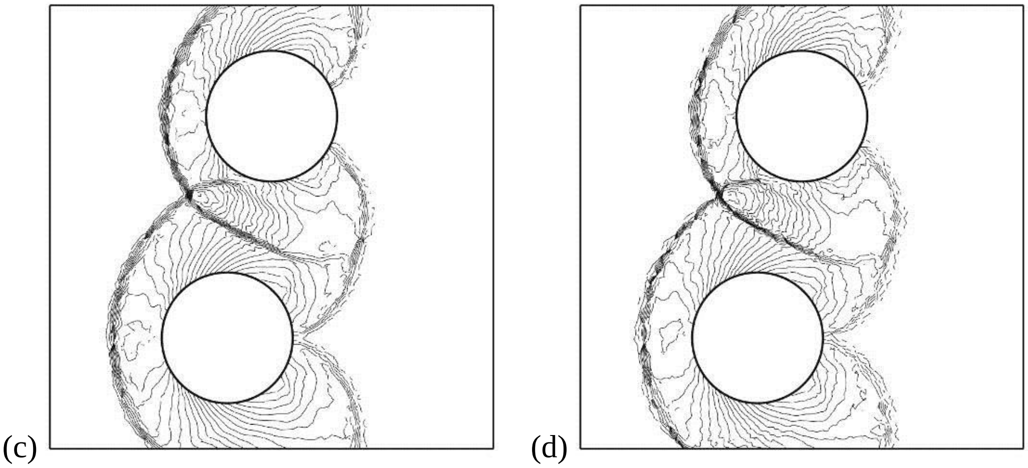

(c) (d)

Figure 21. Results for 2 cylinder Mach reflection case at time=0.16 with no adaptation; (a) base grid (3,740 triangles); (b) 2nd order density contours (11,220 DOFs); (c) 3rd order density contours (22,440 DOFs); (d) 4th order density contours (37,400 DOFs).

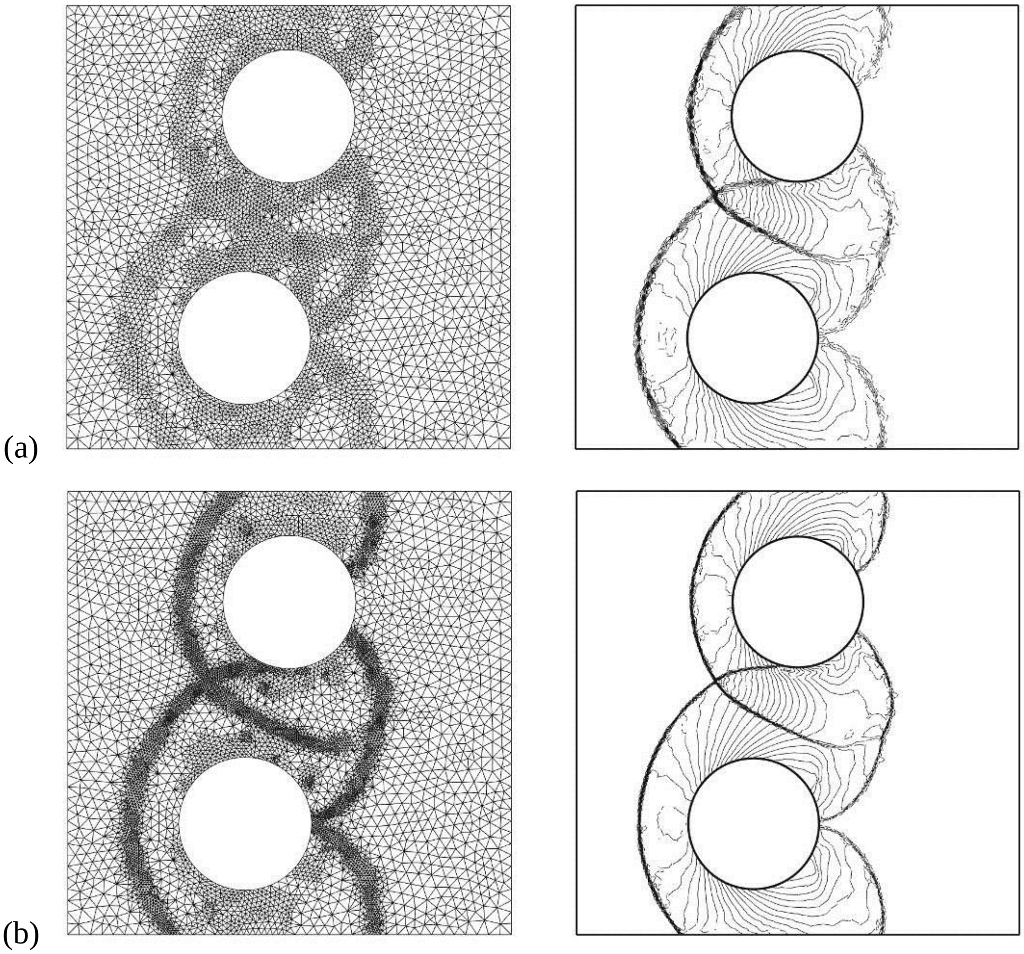

(a)

(b)

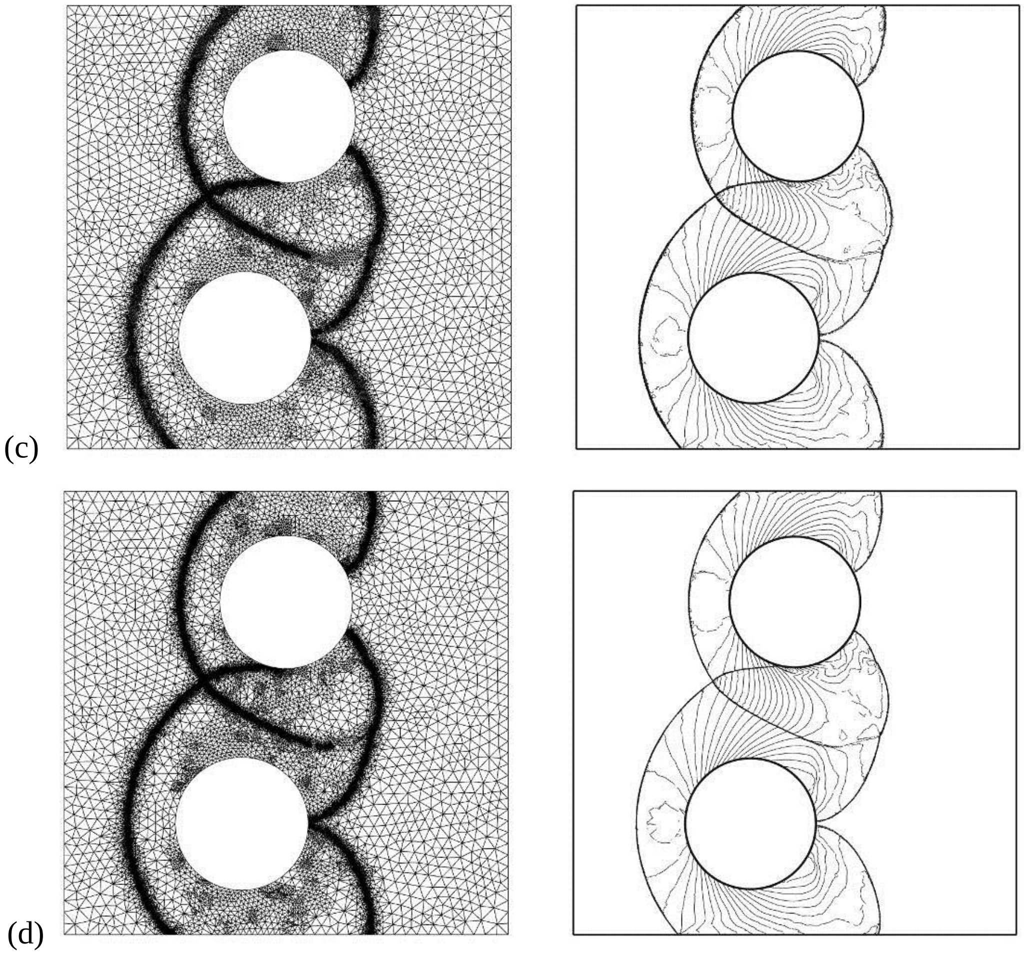

Figure 22. 2nd order grid and density contours for 2 cylinder Mach reflection case at time=0.16; (a) 1 level (22,566 DOFs, 7,522 triangles); (b) 2 levels (39,144 DOFs, 13,048 triangles); (c) 3 levels (71,427 DOFs, 23,809 triangles); (d) 4 levels (134,484 DOFs, 44,828 triangles); Refined from base grid every 100 time steps.

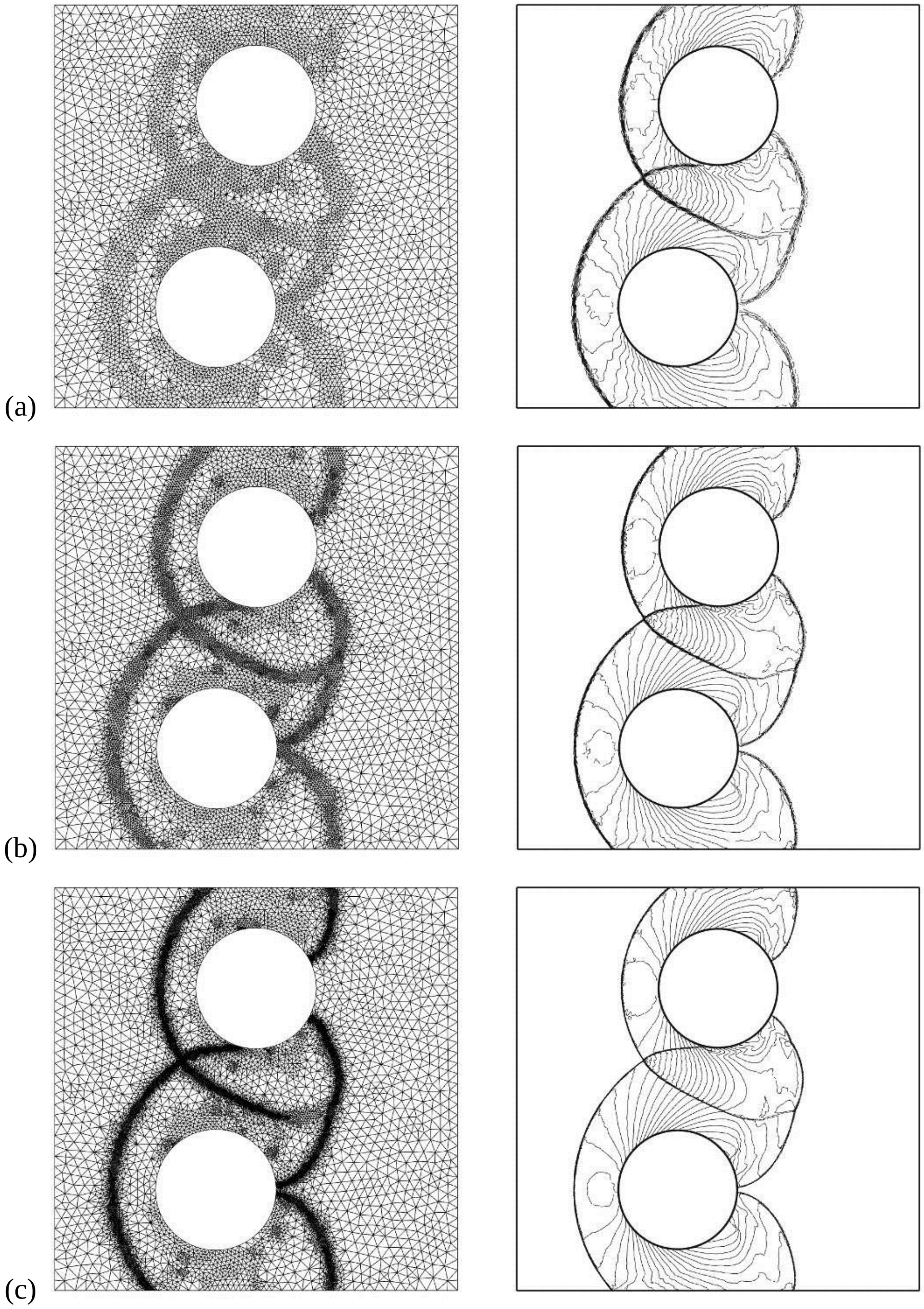

Figure 23. 3rd order grid and density contours for 2 cylinder Mach reflection case at time=0.16; (a) 1 level (45,756 DOFs, 7,626 triangles); (b) 2 levels (78,978 DOFs, 13,163 triangles); (c) 3 levels (143,580 DOFs, 23,930 triangles); Refined from base grid every 100 time steps.

Table I

Initial conditions for RTI problem. The geometric center of the chamber is taken to be the origin of the coordinate system.

Parameter	upper part	lower part
ρ	2	1
u	$\varepsilon_x \sin(8\pi x)\cos[\pi(y+1/2)]\sin^{\tau-1}[\pi(y+1/2)]$	same as upper part
v	$-\varepsilon_y \cos(8\pi x)\sin^{\tau}[\pi(y+1/2)]$	same as upper part
p	$2-2y$	$2-y$

PERSONNEL SUPPORTED

Three graduate students have been supported by this grant, one partially. They are: Rob Harris for the development of quadrature free method, Hong Yang for the extensions to 3D, and Ravi Kannan for the development of an implicit method. Because of the low expenditure in Year 1 (I was not able to find qualified students), we are still catching up in expenditure, and the students are making satisfactory progresses in their research.

In addition, we have established an international collaboration with Tohoku University in Japan. A PhD student, Mr. Takanori Haga, visited ISU between September and November 2006 with his own support to work with my group on jointly developing the SV method. The Tohoku group has been implementing the 3D SV method for the 3D Euler and Navier-Stokes equations on one of the fastest supercomputers in the world, the Earth Simulator, which was the No. 1 computer in the world for several years before several DOE machines surpassed it in speed. The collaboration proved very fruitful for both groups and also leverages the current grant to make faster progress.

PUBLICATIONS AND HONORS

The following journal papers have been published, and DOE's support has been gratefully acknowledged. Other publications are planned.

1. Y. Liu, M. Vinokur, and Z.J. Wang, " Spectral (Finite) Volume Method for Conservation Laws on Unstructured Grids V: Extension to Three-Dimensional Systems," *Journal of Computational Physics* Vol. 212, pp. 454-472 (2006).
2. Y. Sun, Z.J. Wang and Y. Liu, "Spectral (Finite) Volume Method for Conservation Laws on Unstructured Grids VI: Extension to Viscous Flow," *Journal of Computational Physic* Vol. 215, No. 1, pp. 41-58 (2006).
3. Z.J. Wang, Y. Liu, G. May and A. Jameson, "Spectral Difference Method for Unstructured Grids II: Extension to the Euler Equations," *Journal of Scientific Computing*, in press.
4. Y. Sun, Z.J. Wang and Y. Liu, "High-Order Multidomain Spectral Difference Method for the Navier-Stokes Equations on Unstructured Hexahedral Grids", *Communications in Computational Physics*, in press.

The following conference papers have been presented or accepted:

1. R. Harris, Z.J. Wang and Y. Liu, "Efficient Implementation of High-Order Spectral Volume Method for Multidimensional Conservation Laws on Unstructured Grids", accepted by the 45th AIAA Aerospace Sciences Meeting and Exhibits, 2007.
2. Y. Sun, Z.J. Wang and Y. Liu, "Efficient Implicit LU-SGS Scheme for High-Order Spectral Difference Method on Unstructured Hexahedral Grids", accepted by the 45th AIAA Aerospace Sciences Meeting and Exhibits, 2007.
3. H. Yang, R. Harris, Z.J. Wang and Y. Liu, "Efficient Quadrature-Free 3d High-Order Spectral Volume Method On Unstructured Grids," accepted by 18th AIAA CFD Conference, Miami, June 2007.

The PI's recent work on high order methods has gained attention in the international CFD community. For example, a recent review paper in Progress in Aerospace Sciences highlighted the SV method:

John A. Ekaterinaris, "High-order accurate, low numerical diffusion methods for aerodynamics," Vol. 41 No. 3-4, 2005.

In addition, the PI was invited to serve as the Associate Editors of the AIAA Journal and the International Journal of Aerospace Engineering. We are very grateful for DOE's support of the present research.

References

1. R. Abgrall, On essentially non-oscillatory schemes on unstructured meshes: analysis and implementation, J. Comput. Phys. 114 (1994) 45-58.
2. H. L. Atkins, Chi-Wang Shu, Quadrature-free implementation of the discontinuous Galerkin method for hyperbolic equations, AIAA J. 96 (1996) 1683.
3. T. J. Barth, P.O. Frederickson, High-order solution of the Euler equations on unstructured grids using quadratic reconstruction, AIAA Paper No. 90-0013, 1990.
4. B. Cockburn, C.-W. Shu, TVB Runge-Kutta local projection discontinuous Galerkin finite element method for conservation laws II: general framework, Math. Comput. 52 (1989) 411-435.
5. B. Cockburn, S.-Y. Lin, C.-W. Shu, TVB Runge-Kutta local projection discontinuous Galerkin finite element method for conservation laws III: one-dimensional systems, J. Comput. Phys. 84 (1989) 90-113.
6. B. Cockburn, S. Hou, C.-W. Shu, TVB Runge-Kutta local projection discontinuous Galerkin finite element method for conservation laws IV: the multidimensional case, Math. Comput. 54 (1990) 545-581.
7. B. Cockburn, C.-W. Shu, The Runge-Kutta discontinuous Galerkin method for conservation laws V: multidimensional systems, J. Comput. Phys. 141 (1998) 199-224.
8. M. Delanaye, Yen Liu, Quadratic reconstruction finite volume schemes on 3D arbitrary unstructured polyhedral grids, AIAA Paper No. 99-3259-CP, 1999.
9. J. Ekaterinaris, High-order accurate, low numerical diffusion methods for aerodynamics, Progress in Aerospace Sciences 41 (2005) 192-300.
10. J. Flaherty, L. Krivodonova, J.-F. Remacle and M. Shephard, Aspects of discontinuous Galerkin methods for hyperbolic conservation laws. Finite Elements Anal. Design 38 (2002) 889–908.
11. S. K. Godunov, A finite-difference method for the numerical computation of discontinuous solutions of the equations of fluid dynamics, Mat. Sb. 47 (1959) 271.
12. S. Gottlieb, C.-W. Shu, E. Tadmor, Strong stability-preserving high-order time discretization methods, SIAM Rev. 43 (1) (2001) 89-112.
13. T. Haga, N. Ohnishi, K. Sawada, and A. Masunaga, Spectral volume computation of flowfield in aerospace application using Earth simulator, AIAA Paper No.06-2823, 2006.
14. R. Harris, Z. J. Wang, Y. Liu, Efficient quadrature-free high-order spectral volume method on unstructured grids: Theory and 2D implementation, J. Comput. Phys. 227 (2008) 1620-1642.
15. A. Harten, B. Engquist, S. Osher, S. Chakravarthy, Uniformly high order essentially non-oscillatory schemes III, J. Comput. Phys. 71 (1987) 231.
16. J. S. Hesthaven, From electrostatics to almost optimal nodal sets for polynomial interpolation in a simplex, SIAM J. Numer. Anal. Vol. 35 No. 2 (1998) 655-676.
17. C. Hu, C.-W. Shu, Weighted essentially non-oscillatory schemes on triangular meshes, J. Comput. Phys. 150 (1999) 97-127.
18. L. Krivodonova, M. Berger, High-order accurate implementation of solid wall boundary conditions in curved geometries, J. Comput. Phys. 211 (2006) 492-512.
19. Y. Liu, M. Vinokur, Z. J. Wang, Spectral (finite) volume method for conservation laws on unstructured grids V: extension to three-dimensional systems, J. Comput. Phys. 212 (2006) 454-472.

20. J-F Remacle, J.E. Flaherty, M.S. Shephard, An Adaptive Discontinuous Galerkin Technique with an Orthogonal Basis Applied to Compressible Flow Problems, SIAM Review, Vol. 45 No. 1 (2003) 55-73.
21. P. L. Roe, Approximate Riemann solvers, parameter vectors, and difference schemes, J. Comput. Phys. 43 (1981) 357-372.
22. V. V. Rusanov, Calculation of interaction of non-steady shock waves with obstacles, J. Comput. Math. Phys. USSR 1 (1961) 267-279.
23. Y. Sun, Z. J. Wang, Y. Liu, Spectral (finite) volume method for conservation laws on unstructured grids VI: extension to viscous flow, J. Comput. Phys. 215 (2006) 41-58.
24. K. Van den Abeele, T. Broeckhoven, and C. Lacor, Dispersion and Dissipation properties of the 1D spectral volume method and application to a p-multigrid algorithm, J. Comput. Phys. 224 (2) (2007) 616-636.
25. K. Van den Abeele, and C. Lacor, An accuracy and stability study of the 2D spectral volume method, J. Comput. Phys. 226 (1) (2007) 1007-1026.
26. K. Van den Abeele, G. Ghorbaniasl, M. Parsani, and C. Lacor, A stability analysis for the spectral volume method on tetrahedral grids, (submitted to Elsevier Science, 3-17-2008).
27. B. van Leer, Towards the ultimate conservative difference scheme V. a second-order sequel to Godunov's method, J. Comput. Phys. 32 (1979) 101-136.
28. Z. J. Wang, Spectral (finite) volume method for conservation laws on unstructured grids: basic formulation, J. Comput. Phys. 178 (2002) 210.
29. Z. J. Wang, Y. Liu, Spectral (finite) volume method for conservation laws on unstructured grids II: extension to two-dimensional scalar equation, J. Comput. Phys. 179 (2002) 665.
30. Z. J. Wang, Y. Liu, Spectral (finite) volume method for conservation laws on unstructured grids III: extension to one-dimensional systems, J. Sci. Comput. 20 (2004) 137.
31. Z. J. Wang, Y. Liu, Spectral (finite) volume method for conservation laws on unstructured grids IV: extension to two-dimensional Euler equations, J. Comput. Phys. 194 (2004) 716.
32. Z. J. Wang, High-Order Methods for the Euler and Navier-Stokes Equations on Unstructured Grids, Journal of Progress in Aerospace Sciences, Vol. 43 No. 1-3 (2007).
33. S. Wolfram, *Mathematica* Book (Wolfram Media and Cambridge Univ. Press, New York, 1999), 4th Ed.
34. P. Woodward, P. Colella, The Numerical simulation of two-dimensional fluid flow with strong shocks, J. Comput. Phys. 54 (1984) 115-173.
35. M. Zhang, and C-W. Shu, An analysis of and a comparison between the discontinuous Galerkin and the spectral finite volume methods, Computers & Fluids 34 (2005) 581-592.